universität wien

MASTERARBEIT / MASTER'S THESIS

Titel der Masterarbeit / Title of the Master's Thesis

Wells-Dawson phosphotungstates as mushroom tyrosinase inhibitors - A speciation study

verfasst von / submitted by

Raphael Stefan Lampl, BSc

angestrebter akademischer Grad / in partial fulfilment of the requirements for the degree of

Master of Science (MSc)

Wien, 2020 / Vienna 2020

Studienkennzahl lt. Studienblatt / degree programme code as it appears on the student record sheet:	UA 066 862
Studienrichtung lt. Studienblatt / degree programme as it appears on the student record sheet:	Masterstudium Chemie
Betreut von / Supervisor:	Univ.-Prof. Dr. Annette Rompel

Contents

Abbrevations

Å	Ångström
ab	*Agaricus bisporus*
ACN	Acetonitril
ATP	Adensosinetriphosphate
Da	Dalton
ESI-MS	Electrosprayionisation mass spectrometry
FA	Formic acid
FWHM	Full width at half maximum
HIV	Human immunodeficiency virus
HPLC	High pressure liquid chromatography
L-DOPA	*L*-3,4-dihydroxyphenylalanine
LB-media	Lysogeny broth media
LTQ	Linear Trap Quadruple
mM	Millimolar
NMR	Nuclear magnetic resonance
PMSF	Phenylmethylsulfonylfluoride
POM	Polyoxometalate
POMos	Polyoxomolybdates
POT	Polyoxotungstate
PPO	Polyphenol oxidase
UV-VIS	Ultraviolet-visible

Preface

In this master thesis, four different polyoxotungstates were tested for inhibition against *agaricus bisporus* polyphenoloxidase four. After recombinant expression the enzyme was purified and activated with Proteinase K. The activity of the enzyme in the presence of polyoxotungstates was followed via spectroscopic measurements. The stability of polyoxotungstates under physiological conditions was analyzed with nuclear magnetic resonance measurements. Both inhibition type and inhibition constant were evaluated. The thesis is presented as a cumulative study and begins with an introduction to the interdisciplinary topic, which is followed by a submitted paper to a scientific journal.

Publication

as main author:

Lampl, R.; Breibeck, J., Gumerova, I.N., Galanski M.; Rompel A.; Wells-Dawson phoshotungstates as mushroom tyrosinase inhibitors – A speciation study

Submitted to Scientific Reports on February 16th 2020.

1. Motivation and Aim

Recent studies demonstrated that polyoxometalates (POMs) have a broad range of applications in catalysis, protein crystallization (e.g. $[TeW_6O_{24}]^{6-}$ as co-crystallization agent of latent *Agaricus bisporus* polyphenoloxidase 4), and in biochemistry. POMs show anti-HIV, anti-bacterial, anti-virus or anti-diabetes effects, due to their wide spectrum of structure, shape and properties. However, the mechanism with biomolecules often is unknown.

It was shown that the Wells-Dawson polyoxometalate $K_6[\alpha\text{-}P_2W_{18}O_{62}]\cdot 14H_2O$ has good inhibition effects against the signal transport protein Ca^{2+}-ATPase (*Gumerova et al.*, 2017). Moreover, for high affinity polyoxometalates (*i.e.* Wells-Dawson $K_6[\alpha\text{-}P_2W_{18}O_{62}]\cdot 14H_2O$ and $K_{12}[\alpha\text{-}H_2P_2W_{12}O_{48}]\cdot 16H_2O$) there is a relation between charge-density (charge divided by volume in $Å^3$) and inhibitory effect.

Experiments by *Gumerova et al.* (2018) revealed that the Wells-Dawson archetype POMs show good anti-bacterial properties against bacteria *Moraxella catarrhalis,* which indicates further polyoxometalate-protein interaction.

Moreover, in 2019 *Breibeck et al.* investigated the charge-dependent inhibition of Keggin-type polyoxometalates on *agaricus bisporus* (mushroom) polyphenoloxidase four.

In the present study, Wells-Dawson $[\mathbf{P_2W_{18}}]^{6-}$, and the related lacunary anions $[\mathbf{P_2W_{17}}]^{10-}$, $[\mathbf{P_2W_{15}}]^{12-}$, $[\mathbf{P_2W_{12}}]^{12-}$ are tested against *agaricus bisporus* (mushroom) polyphenoloxidase four to explore their inhibitory effect and to obtain a deeper understanding of the inhibiting mechanism. Other than in previous surveys, the composition of the Wells-Dawson POTs under physiological conditions via ^{31}P- and ^{183}W- NMR spectroscopy is studied.

The aim of this thesis is to get fundamental knowledge of the interaction between Wells-Dawson archetype POTs with polyphenoloxidase four from mushroom. Inhibition curves and Lineweaver-Burk plots provide insight into the inhibitory strength (*i.e.* K_i -values and α-parameter) of the inhibitor. The NMR spectra give an outlook for the testing of further POT - *ab*PPO4 interaction in coming studies.

2. Introduction

2.1. *Agaricus bisporus* Polyphenoloxidase 4 (*ab*PPO4)

*Ab*PPO4 (*agaricus bisporus*) is a copper containing metalloenzyme of the family of polyphenoloxidases, with catalytic activity in the melanin biosynthesis of white button mushroom. The enzyme catalyzes the *o*-hydroxylation of monophenols to *o*-diphenols (monophenolase or cresolase activity) and the subsequent oxidation of *o*-diphenols to *o*-quinones (diphenolase or catechol oxidase activity). It has a type three copper center and the fully oxidized state (*oxy* form) of the protein contains dioxygen in "side-on" bridging mode (μ-η^2:η^2). In *ab*PPO4, the C-terminus forms a cap for the active center and has to be removed to transfer the enzyme from its latent to the permanently active form.

2.2. Polyoxometalates (POM)

Polyoxometalates (POMs) are negatively charged metal cluster compounds built up of MO_6 octahedra. M is the so called addenda atom, which in mostly W, Mo, or V in a high oxidation state. POMs have a vast spectrum of applications in computer science, catalysis, protein crystallography, material science and biochemistry. There are several archetypes of POMs, for example Lindquvist, Anderson, Keggin or Wells-Dawson.

Wells-Dawson POMs form different isomers, where the three edge-sharing octahedra of a triad at the top or bottom ("cap") are rotated by π/3 (60°). The different isomers are denoted as α-, β-, and γ-isomer, and additional rotation of the six corner-sharing oxtahedra yields the α*-, β*-, and γ*-isomers. POMs can be hydrolyzed to have vacant ("lacunary") positions, where α_1- indicates a missing octahedron in the middle plane ("belt") and α_2 denotes a missing octahedron at the "cap". The synthesis of most polyoxotungstates works with reflux heating of orthotungstate and inorganic acid. Through varying pH-value, temperature and reflux time different archetypes can be synthesized. In aqueous solution, they are stable at low pH values (*e.g.* pH = 2) and decompose at higher pH values (*e.g.* pH = 6.8). The tungsten atoms in POTs can easily take up electrons, which is reflected in the blue colour of the reduced form ("heteropoly blues").

2.3. Nuclear Magnetic Resonance spectroscopy (NMR-spectroscopy)

NMR spectroscopy is a method to study the structure (*e.g.* biomolecules, organic or inorganic molecules) and dynamics (equilibrium or far from equilibrium) of chemical compounds, using the nuclear core spin of an NMR-active isotope. The only nuclear cores which are not NMR-active have an even number of protons and even mass number.

A magnetic field is applied to the sample, which splits the quantum energetic level of the core spin into an upper and a lower level. Afterwards, transitions from the lower to the upper spin state are excited by radio waves. The energy difference of the spin states ΔE is given by

$$\Delta E = \gamma \hbar B_0 = h\nu \quad (1)$$

γ is the gyromagnetic ratio of an isotope, $\hbar$ is the Plancks constant divided by 2π, B_0 is the magnetic field of the spectrometer and ν is the frequency of the radio waves.

The core spin depends on the measured element and on its chemical neighborhood. For the interpretation of NMR-spectra, the chemical shift is calculated via

$$\delta = \frac{\delta_{sample} - \delta_{reference}}{\delta_{reference}}. \quad (2)$$

If the chemical shift is lowered with regard to a standard reference signal, it is called upfield shift (high field), otherwise it is called downfield shift (low field). In POM chemistry, ^{31}P-, ^{51}V-, ^{95}Mo- or ^{183}W-NMR are often used to explore the structure of the clusters by the symmetry positions of addenda and heteroatoms.

3. Major results

3.1. Kinetic measurements

The diphenolase activity (catechol oxidase activity) of *ab*PPO4 was assayed with *L*-DOPA (*L*-3,4-dihydroxyphenylalanine). The measurements were taken in triplicates. Non-linear regression, with starting values for K_i and the α-parameter from Lineweaver-Burk plots, was used to obtain activity curves of the enzyme in the presence of POT inhibitors. These hyperbolic functions showed a kindred shape, hinting to a similar response mechanism for the different POTs. The three Lineweaver-Burk lines of each tested Wells-Dawson POT intersected in the third quadrant, exhibiting mixed-type inhibition. According to a hyberbolic curve fit with OriginPro 8, $[\mathbf{P_2W_{17}}]^{10-}$ had the greatest inhibitory activity (K_i = 6.53 mM) followed by $[\mathbf{P_2W_{12}}]^{12-}$ (K_i = 7.50 mM), $[\mathbf{P_2W_{18}}]^{6-}$ (K_i = 9.65 mM) and $[\mathbf{P_2W_{15}}]^{12-}$ (K_i = 13.63 mM).

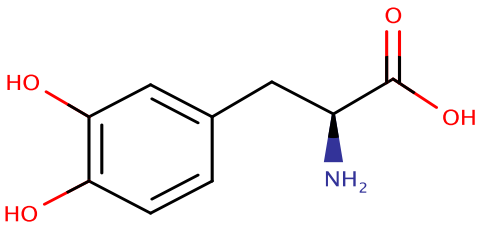

Illustration 1. Structural formula of substrate *L*-DOPA (*L*-3,4-dihydroxyphenylalanine)

3.2. Speciation of POT inhibitors with ^{183}W-NMR and ^{31}P-NMR

To obtain crucial insight into the actual POT composition in solution, NMR-spectroscopy of tungsten-183 and phosphorus-31 was performed. The measurements were carried out at biological conditions (pH 6.8). The ^{183}W-NMR spectra confirmed the POT speciation from the ^{31}P-NMR. $[P_2W_{17}O_{61}]^{10-}$ was the main species found in all NMR-spectra without addition of substrate. Via integration of the ^{31}P-NMR peaks of the monolacunary form, the following

amounts of the main species in the POT samples were derived: $[\mathbf{P_2W_{12}}]^{12-}$(~76.9%)<$[\mathbf{P_2W_{15}}]^{12-}$(~82.4%)<$[\mathbf{P_2W_{18}}]^{6-}$(~97.8%)<$[\mathbf{P_2W_{17}}]^{10-}$(100%).

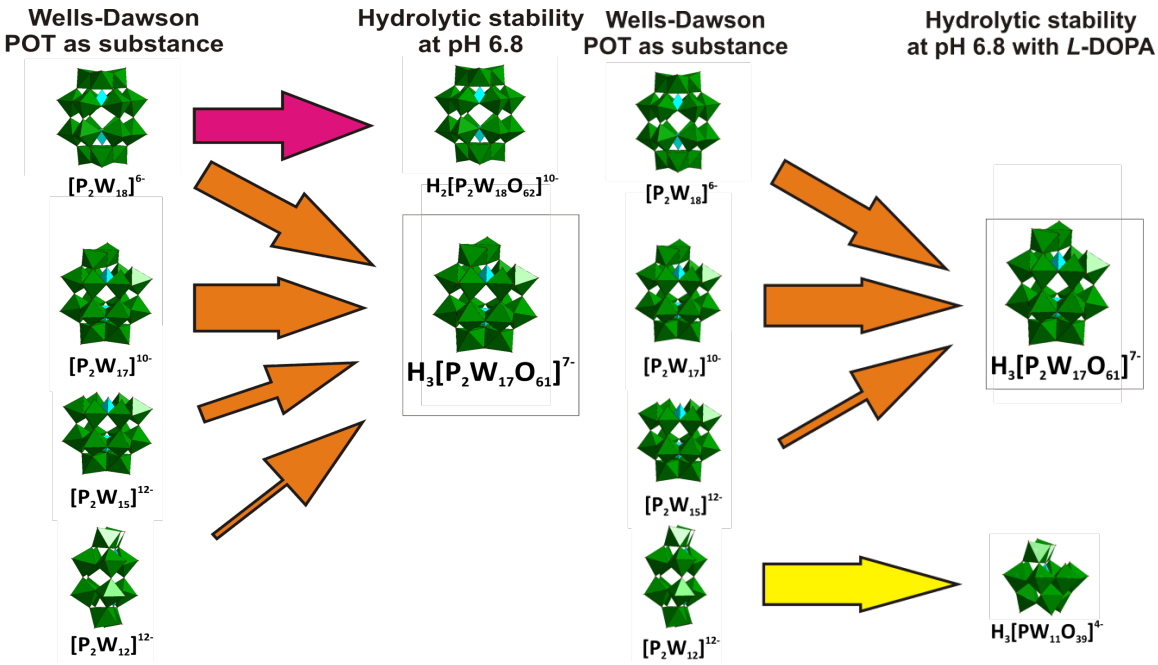

Illustration 2. Overview of NMR-spectroscopy measurements without and with addition of *L*-DOPA. At pH 6.8, $H_3[P_2W_{17}O_{61}]^{7-}$ was the main species, which could be found in all samples. As predicted by the literature, $[P_2W_{18}O_{62}]^{10-}$ is not stable at pH 6.8.

After addition of substrate to $[\mathbf{P_2W_{18}}]^{6-}$, the solution turned blue. Therefore, subsequent NMR measurements with the addition of substrate to the POT solutions were undertaken, revealing rearrangement in $[\mathbf{P_2W_{12}}]^{12-}$ to $H_3[PW_{11}O_{39}]^{4-}$.

3.3. Charge density dependence on inhibitory effects of Wells-Dawson POT species

Furthermore, the charge density concept was introduced to describe the inhibitory activities of the phosphotungstates. The charge of the POT compounds (q) was divided by the number of tungsten addenda atoms (m) to obtain the charge density (q/m). The charge density is influenced by protonation and reduction of the POT, where the protonation state was taken from the literature. The monolacunary species $[P_2W_{17}O_{61}]^{10-}$ (Wells-Dawson) and $[PW_{11}O_{39}]^{7-}$ (Keggin) are reported to take up three protons in the neutral pH range. Considering that, the charge densities of the most inhibiting species were q/m = 0.36 for $H_3[PW_{11}O_{39}]^{4-}$ (K_i = 7.50 mM,) and q/m = 0.41 for $H_3[P_2W_{17}O_{61}]^{7-}$ (K_i = 6.53 mM,), respectively. Therefore, the similar charge densities explain the inhibitory effects of the POTs closely resembling each other.

4. Publication

4.1. Title

Wells-Dawson phosphotungstates as mushroom tyrosinase inhibitors - A speciation study

Raphael Lampl[1], Joscha Breibeck[1], Nadiia I. Gumerova[1], Markus Galanski[2] and Annette Rompel*[1]

[1] Universität Wien, Fakultät für Chemie, Institut für Biophysikalische Chemie, Althanstraße 14, 1090 Wien, Austria; https://www.bpc.univie.ac.at

[2] Universität Wien, Fakultät für Chemie, Institut für Anorganische Chemie, Währinger Str. 42, 1090 Wien, Austria.

**Correspondence to: annette.rompel@univie.ac.at*

4.2. Abstract

The polyphenol oxidase from mushroom (*ab*PPO4) performs mono- and diphenolase reactions and its activity has been inhibited by polyoxometalates. In the present work, the diphenolase activity of *ab*PPO4 is targeted at pH 6.8 by the four Wells-Dawson phosphotungstates $[P_2W_{18}O_{62}]^{6-}$, $[P_2W_{17}O_{61}]^{10-}$, $[P_2W_{15}O_{56}]^{12-}$ and $[H_2P_2W_{12}O_{48}]^{12-}$ in order to elucidate their structure-activity relationship. Kinetic data were obtained from the dopachrome assay for evaluation of the inhibition parameters according to a generalized Michaelis-Menten model and Lineweaver-Burk plots. The monophasic inhibition behavior was confirmed by a Hill-based algorithm. The speciation in the tested polyoxotungstates (POTs) solutions at the dopachrome assay conditions was identified by ^{183}W-NMR and ^{31}P-NMR spectroscopy, facilitating a straightforward assignment of inhibition effects to the identified POT species. The inhibitory activity of Wells-Dawson phosphotungstates is correlated to the degree of their relative rearrangement to $[P_2W_{17}O_{61}]^{10-}$. Without addition of the substrate (*L*-DOPA), $[P_2W_{18}O_{62}]^{6-}$, $[P_2W_{15}O_{56}]^{12-}$ and $[H_2P_2W_{12}O_{48}]^{12-}$ exhibit partial disintegration to the monolacunary $[P_2W_{17}O_{61}]^{10-}$ anion, while $[P_2W_{17}O_{61}]^{10-}$ retained its structural integrity exhibiting the strongest binding to the enzyme (K_i = 6.53 mM). In the presence of *L*-DOPA, only $[H_2P_2W_{12}O_{48}]^{12-}$ changes its speciation and converts to the Keggin type anion $[PW_{11}O_{39}]^{7-}$ (K_i = 7.50 mM). The tight binding and consequently good inhibitory effect of the Wells-Dawson $H_3[P_2W_{17}O_{61}]^{7-}$ and Keggin $H_3[PW_{11}O_{39}]^{4-}$ anions is explained by their low charge density values (q/m = 0.41 and 0.33, respectively).

4.3. Introduction

Polyphenol oxidases (PPO) are omnipresent copper-containing proteins present in animals, fungi, plants and bacteria[1,2,3], with tyrosinases and catechol oxidases being prominent members of this enzyme family. Tyrosinases exhibit cresolase activity (EC 1.14.18.1; *ortho*-hydroxylation of monophenols to *ortho*-diphenols, monophenolase activity) and catecholase activity (EC 1.10.3.1; oxidation of *ortho*-diphenols to *ortho*-quinones; diphenolase activity) and give rise to the rate determining step in the melanogenesis of mushrooms involved in pigment coating and browning[4]. For its negligible lag phase and generally faster reaction velocity, the diphenolase activity of tyrosinases is usually assayed using *L*-DOPA (*L*-3,4-dihydroxyphenylalanine, Figure S1 A), as the substrate for the dopachrome assay[5]. The POT inhibition parameters were determined by fitting the kinetic data to a generalized Michaelis-Menten model and Lineweaver-Burk plots, accompanied by POT speciation studies applying ^{31}P-NMR and ^{183}W-NMR under physiological conditions (pH 6.8) with or without the substrate *L*-DOPA. The strongest mushroom PPO inhibitor is the structurally related kojic acid (Figure S1 B), which holds inhibition constant (K_i) values in the µM range[6] and acts as a competitive inhibitor6. Mushroom (*Agaricus bisporus*; abbr: *ab*) PPO is present in great quantity in fruiting bodies[7]. The enzyme has been thoroughly characterized in its structure[8,9] and activity[10]. Following the established protocol by Pretzler *et al.*[11], *ab*PPO4 was recombinantly expressed in *E. coli*, purified in its active form and used in inhibition studies.

Polyoxometalates (POMs) are metal-oxygen clusters commonly built up by W, Mo or V addenda atoms, which are usually in their highest oxidation states exhibiting the electronic configuration d^0 or d^1 [12]. POMs show a widespread biological applicability such as antibacterial[13] and anti-tumor activity[14], and stable polyoxotungstates (POTs) have successfully been applied as additives in co-crystallization experiments with proteins[15, 16, 17]. Apart from the Anderson-Evans archetype[18] (e.g. $[TeW_6O_{24}]^{6-}$ is stable in aequous solution between pH 4.5 and 7.5), most POTs show low pH stability at physiological conditions, requiring solution NMR-measurements to reveal the true composition under the applied conditions. As POTs possess a higher chemical stability than polyoxomolybdates (POMos), tungsten is usually selected as the addenda atom in biological investigations.

Recently, a systematic approach varying the charge density in a series of Keggin polyoxotungstates (POTs) was reported by Breibeck *et al.*[19] to characterize their inhibitory effects against recombinant *ab*PPO4[11]. A detailed assignment of the active Keggin POT species was undertaken applying NMR spectroscopy[19]. A charge dependence of the inhibitory capacities was derived, where the inhibitory effect is reversely related to the net charge of the POT species. The most active Keggin POT was $[SiW_{12}O_{40}]^{4-}$ (K_i = 4.7 mM), but the more stable anions with higher charge density did not reduce the enzymatic activity.

Another prominent POM scaffold investigated for biological activity is the Wells-Dawson archetype with the general formula $[(X^{n+})_2M_{18}O_{62}]^{(16-2n)-}$ [20], where M is either W or Mo and X^{n+} is commonly phosphorus(V) or arsenic(V). For the intact form of this cluster, 18 MO_6 octahedral units enclose both inner heteroatom groups $\{XO_4\}$ by corner and edge-sharing (Figure 1). Wells-Dawson POMs exhibited antibacterial activity[21], and both the intact anion and the hexalacunary form showed inhibition against Ca^{2+}-ATPase and P-type ATPase[22]. Wells-Dawson POMos were used as inhibitors against α-glucosidase with K_i-values covering a wide range down to the µM scale[23].

In this study, the inhibitory effect of four structurally related Wells-Dawson POTs $Cat_6[P^V_2W^{VI}_{18}O_{62}]\cdot 14H_2O$ (Cat = K^+, NH_4^+) [24, 25], $K_{10}[\alpha_2\text{-}P^V_2W^{VI}_{17}O_{61}]\cdot 20H_2O$ [25, 26], $K_{12}[P^V_2W^{VI}_{15}O_{56}]\cdot 24H_2O$ [26, 27] and $(NH_4)_{12}[H_2P^V_2W^{VI}_{12}O_{48}]\cdot 24H_2O$ [28, 29] (Table S2) with formal net charges from 6- to 12- on the catecholase activity of *ab*PPO4 was explored (Figure 1). For the inhibition studies, the POTs were buffered at pH 6.8 in 50 mM Na-citrate and the resulting samples in solution are termed $[\mathbf{P_2W_{18}}]^{6-}$ for $K_6[P^V_2W^{VI}_{18}O_{62}]\cdot 14H_2O$ and $(NH_4)_6[P^V_2W^{VI}_{18}O_{62}]\cdot 14H_2O$, $[\mathbf{P_2W_{17}}]^{10-}$ for $K_{10}[\alpha_2\text{-}P^V_2W^{VI}_{17}O_{61}]\cdot 20H_2O$, $[\mathbf{P_2W_{15}}]^{12-}$ for $K_{12}[P^V_2W^{VI}_{15}O_{56}]\cdot 24H_2O$ and $[\mathbf{P_2W_{12}}]^{12-}$ for $(NH_4)_{12}[H_2P^V_2W^{VI}_{12}O_{48}]\cdot 24H_2O$ to distinguish the buffered sample from the solid compound. The focus was on the identification of the active species present under biological conditions that inhibit the diphenolase activity. Therefore, the charge density was systematically varied by lacunarization, i.e. by stepwise removal of WO_x entities.

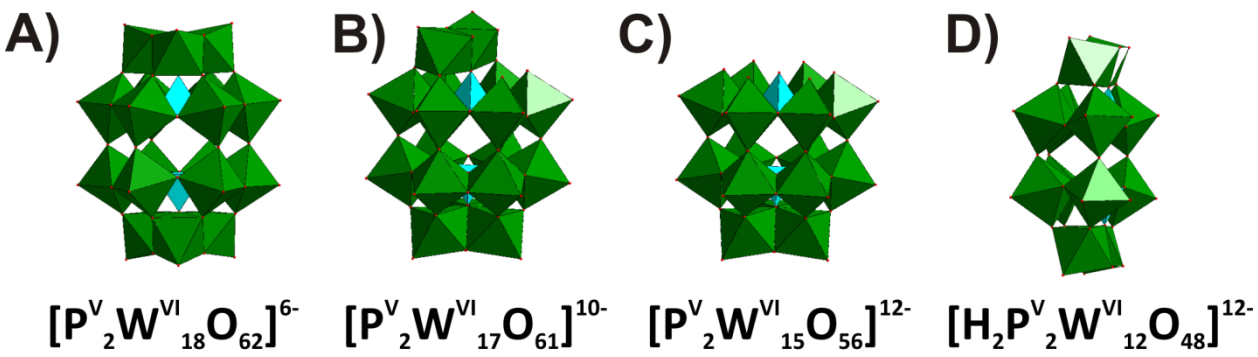

Figure 1. The POTs A)-D) feature the Wells-Dawson archetype and they are derived from the *α*-isomer of $[P_2W_{18}O_{62}]^{6-}$. Colour code*:* $\{WO_6\}$ octahedra, green; $\{PO_4\}$ tetrahedral, turquoise.

4.4. Results and Discussion

4.4.1. Activity plots of abPPO4 inhibited by Wells-Dawson POTs

*Ab*PPO4 was purified and activated according to Pretzler *et al.*[11] The ESI-MS of active *ab*PPO4 is presented in Figure S2 and Table S1 and the SDS-PAGE analysis of *ab*PPO4 is shown in Figures S4 and S5. The protocols for the synthesis of the Wells-Dawson POTs were taken from published procedures (cf. Table S2) and their identity was confirmed by IR in solid state (Figure

S6). For the investigation of potential inhibition of *ab*PPO4 by the Wells-Dawson POTs, they were dissolved at pH 6.8 in 50 mM Na-citrate buffer ($[\mathbf{P_2W_{18}}]^{6-}$, $[\mathbf{P_2W_{17}}]^{10-}$, $[\mathbf{P_2W_{15}}]^{12-}$, $[\mathbf{P_2W_{12}}]^{12-}$) and the diphenolase activity of the tyrosinase was monitored using 1 mM *L*-DOPA as the substrate. The concentration of the investigated Wells-Dawson phosphotungstates was in the range 0–5 mM. If enzymatic inhibition was observed, data were taken in triplicates and fitted with a hyperbolic function (cf. SI equation (5)) from a mixed inhibition model to evaluate the K_i and α-parameters. All four tested solutions $[\mathbf{P_2W_{18}}]^{6-}$, $[\mathbf{P_2W_{17}}]^{10-}$, $[\mathbf{P_2W_{15}}]^{12-}$ and $[\mathbf{P_2W_{12}}]^{12-}$ exhibited the mixed-type inhibition with K_i values in the mM range, binding both to the free enzyme and to the enzyme-substrate complex[30] (Table 1, Figure 2). As a positive control for the inhibition of *ab*PPO4 diphenolase activity and for validation of the kinetic methodology, the well-characterized natural PPO-inhibitor kojic acid was additionally tested and evaluated applying exactly the same mathematical model. This organic inhibitor features a K_i in the µM range corresponding to a much higher affinity to the enzyme as revealed for the Wells-Dawson phosphotungstates. To investigate the effect of POT charge density (POT charge *q* divided by the number of tungsten atoms *m*, Tables 2, S3)[31], the inhibitory data for the lacunary Keggin POT $[PW_{11}O_{39}]^{7-}$ [32] ($[\mathbf{PW_{11}}]^{7-}$), which was previously tested under the same conditions,[19] were compared with the data obtained in this study.

Table 1. Summary of kinetic evaluation of *ab*PPO4 inhibition by Wells-Dawson POTs. K_i: inhibition constant. α: inhibition parameter, R^2: curve fit determination coefficient; the parameters were determined [a] from activity plot and [b] from the Lineweaver-Burk slopes or intercepts.

Effector	K_i [mM]	α	R^2	Inhibition type
$[\mathbf{P_2W_{18}}]^{6-}$	9.65[a], 12.96[b]	0.013[a], 0.219[b]	0.80	Mixed-type
$[\mathbf{P_2W_{17}}]^{10-}$	6.53[a], 10.63[b]	0.01[a], 0.01[b]	0.93	Mixed-type
$[\mathbf{P_2W_{15}}]^{12-}$	13.63[a], 10.74[b]	0.003[a], 0.2[b]	0.96	Mixed-type
$[\mathbf{P_2W_{12}}]^{12-}$	7.50[a], 5.61[b]	0.017[a], 0.28[b]	0.91	Mixed-type
Control: kojic acid [6,19]	4.5[a], 4.3[b] µM	$2.6 \cdot 10^{15}$	1.0	Competitive
Control: $[\mathbf{PW_{11}}]^{7-}$ [19]	12.0[a], 9.9[b]	0.12[a], 0.17[b]	0.91	Mixed-type

To evaluate the inhibitory effect, the activity plots for four Wells-Dawson phosphotungstates were plotted in the concentration range 0–5 mM (Figure 2). The four inhibition curves show a highly similar shape, suggesting the responsible POT species in solution to be very similar or even identical. Among the Wells-Dawson clusters, $[\mathbf{P_2W_{17}}]^{10-}$ showed the greatest inhibitory effect (K_i = 6.53 mM) and the fitted α-parameter suggests a mixed mode of inhibition (Table 1). According to K_i values $[\mathbf{P_2W_{17}}]^{10-}$ (K_i = 6.53 mM) and $[\mathbf{P_2W_{12}}]^{12-}$ (K_i = 7.50 mM) exhibited nearly identical inhibitory activity. $[\mathbf{P_2W_{18}}]^{6-}$ (K_i = 9.65 mM) and $[\mathbf{P_2W_{15}}]^{12-}$ (K_i = 13.63 mM) showed a lower inhibition capacity. These findings hint towards expectable structural changes of the phosphotungstates at physiological pH 6.8, which are addressed by ^{31}P-NMR and ^{183}W-NMR-POT speciation studies (see Figure 3 and explanation as well as Section 4, 5 in SI).

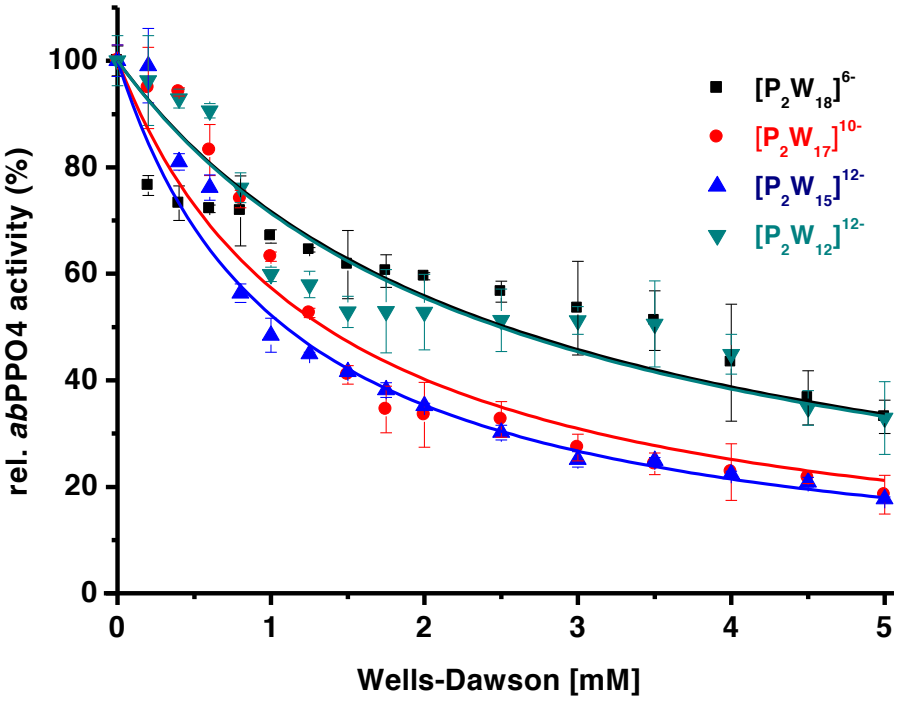

Figure 2. Activity plots of *ab*PPO4 with four Wells-Dawson phosphotungstates. The dopachrome assay was performed using 1 mM *L*-DOPA as the substrate in 50 mM Na-citrate buffer at pH 6.8. The measurements were taken in triplicates and a hyperbolic curve fit (equation (5), SI) was performed. The parameters are summarized in Table 1.

4.4.2. Determination of inhibition modes for effective compounds

The type of enzymatic inhibition is usually investigated by linear plots according to Lineweaver-Burk, also allowing for further validation of the inhibitory constant K_i. For each of the four Wells-Dawson clusters as well as the kojic acid control measured in our previous study[19], the dopachrome assay was repeated at five different substrate concentrations (varying from 0.4 to 2 mM) and three different inhibitor concentrations, respectively (SI section 7, Figures S13-S16, Tables S4, S5).

4.4.3. Lineweaver-Burk evaluation of inhibition types

To determine the kind of inhibition, Lineweaver-Burk plots were generated from the reaction velocities obtained at five different substrate concentrations (0.4-1.5 mM) and three different POT concentrations (0-6 mM), respectively (Figures S13-S16). Each POT analysis yielded a set of three lines intersecting in a common point. The slopes (SI equation (13), insets in Figures S13-S16) and ordinate intercepts of these lines were further evaluated to validate the inhibitory constant K_i and the α-parameter from the non-linear regression procedure. Therefore, the slopes were plotted against the used inhibitor concentrations to give lines intersecting the abscissa at $-K_i$. Similarly, the Lineweaver-Burk ordinate intercepts were evaluated for the α parameter (cf. Table S5 and Table 1). In good accordance with their structural similarity, the respective intersection point of the three Lineweaver-Burk lines was found in the third quadrant

for all four Wells-Dawson POTs tested here, which indicated mixed-type inhibition.[30, 33] The same inhibition behavior with *ab*PPO4 was exhibited by Keggin POTs before[19].

4.4.4. Speciation of Wells-Dawson POT by ^{183}W-NMR and ^{31}P-NMR analyses at pH 6.8

The stability of Wells-Dawson phosphotungstates was not accurately verified in most biological application studies reported so far. However, the detailed structural information about species under the respective experimental conditions is essential for understanding of POM activity.

All Wells-Dawson POTs were dissolved in reaction buffer (50 mM Na-citrate, pH 6.8) and were adjusted with 1 M HCl or 1 M NaOH to pH 6.8 for measurements with *ab*PPO4. Upon dissolution of $[\mathbf{P_2W_{18}}]^{6-}$ and $[\mathbf{P_2W_{17}}]^{10-}$, the physiological pH of the buffer slightly decreased, whereas $[\mathbf{P_2W_{15}}]^{12-}$ and $[\mathbf{P_2W_{12}}]^{12-}$ behaved as strong bases.

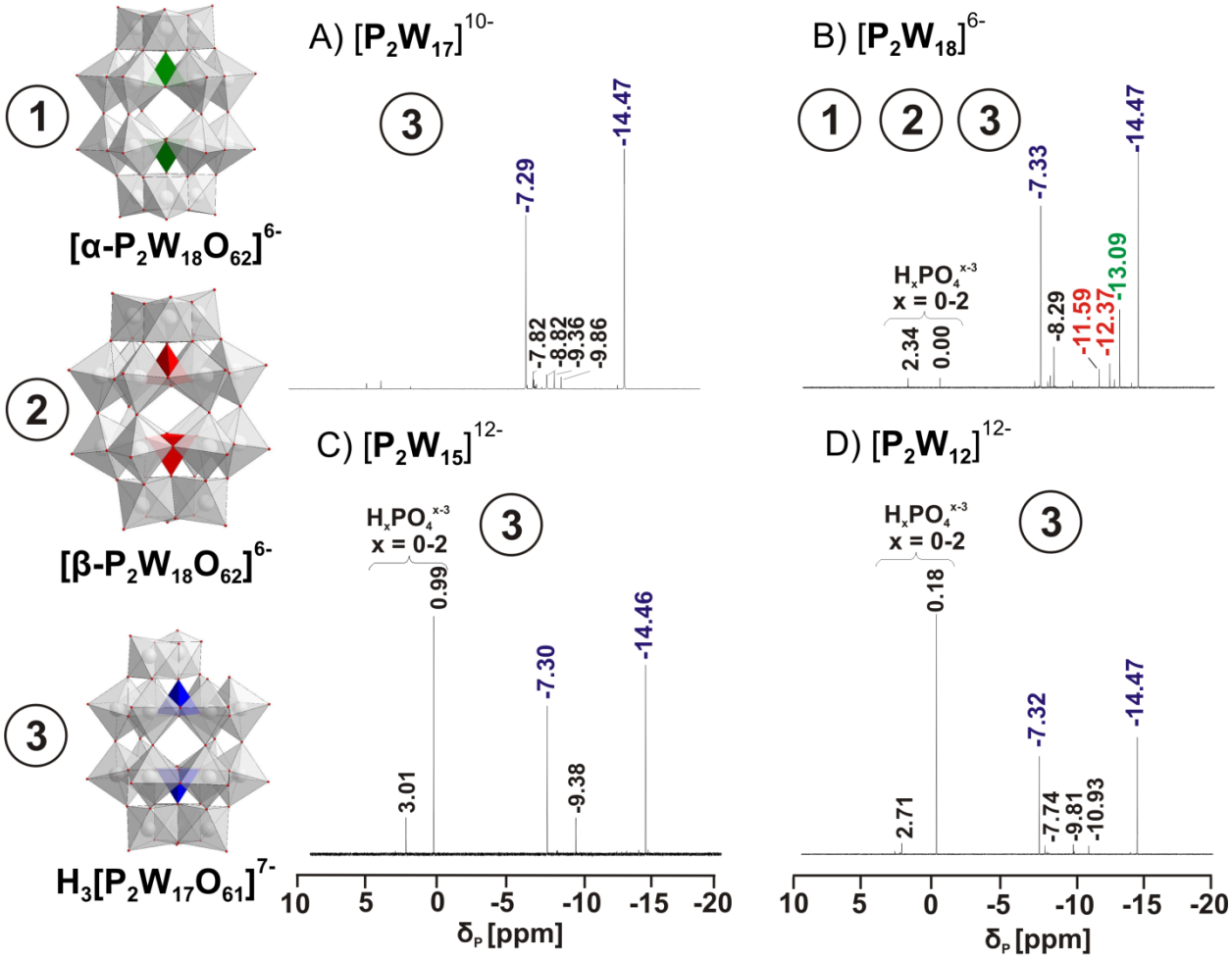

Figure 3. ^{31}P-NMR spectra of $[\mathbf{P_2W_{18}}]^{6-}$, $[\mathbf{P_2W_{17}}]^{10-}$, $[\mathbf{P_2W_{15}}]^{6-}$ and $[\mathbf{P_2W_{12}}]^{12-}$ at pH 6.8 (Table S3). The assignable educts and products of the hydrolytic rearrangement reactions of the respective POTs (approximately 20 mM) under the given buffer conditions are depicted to illustrate the sample speciation. A) educt/product $H_3[P_2W_{17}O_{61}]^{4-}$ B) educts: $H_2[\alpha\text{-}P_2W_{18}O_{62}]^{10-}$ and $H_2[\beta\text{-}P_2W_{18}O_{62}]^{10-}$ on the left side; product: $H_3[P_2W_{17}O_{61}]^{4-}$ on the right side; C) product: $H_3[P_2W_{17}O_{61}]^{4-}$; D) product: $H_3[P_2W_{17}O_{61}]^{4-}$; Signal assignment according to ref. [34]. Colour code: {WO_6} octahedra, white; {PO_4} tetrahedra, blue, green, red; O atoms, red.

^{183}W-NMR in combination with ^{31}P-NMR is established as a useful technique to determine the structural composition of POTs[12] and was successfully applied for Keggin clusters speciation in an analogous study.[19] To verify the identity of $[P^{V}_{2}W^{VI}_{18}O_{62}]^{6-}$ and its stability at pH 4, where the intact anion has been reported to be stable, NMR-measurements were performed (Figure S7, S10). The analysis of the spectra identified the α-isomer (two ^{183}W-signals; one ^{31}P signal) and small amounts (~20 % according to signals intensities) of β-isomer (four ^{183}W-signals; two ^{31}P signals). At the experimental conditions (50 mM Na-citrate, pH 6.8), the predominant species is $[P_2W_{17}O_{61}]^{10-}$ (nine ^{183}W-signals; two ^{31}P signals) for all four tested compounds. In aqueous solution at pH 6.8, $[\mathbf{P_2W_{18}}]^{6-}$ showed partial hydrolysis of $[P^{V}_{2}W^{VI}_{18}O_{62}]^{6-}$ to $[P^{V}_{2}W^{VI}_{17}O_{61}]^{10-}$ (Figure 3 B, S8 B), $[\mathbf{P_2W_{17}}]^{10-}$ exhibited $[P^{V}_{2}W^{VI}_{17}O_{61}]^{10-}$ as the only present species (Figure 3 A, S8 A), whereas in the ^{183}W- and ^{31}P-NMR spectra for $[\mathbf{P_2W_{15}}]^{12-}$ (Figure 3 C, S8 C) and $[\mathbf{P_2W_{12}}]^{12-}$ (Figure 3 D, S8 D) rearrangement to $[P_2W_{17}O_{61}]^{10-}$ was observed (Figure 3, S8).

In every ^{31}P-NMR analysis, peaks for free phosphate were observed, indicating the release of $H_xPO_4^{x-3}$ from the POT clusters as a consequence of partial decomposition or rearrangement (Figure 3 B-D). The comparison of the integrated ^{31}P-NMR peaks for $[P^{V}_{2}W^{VI}_{17}O_{61}]^{10-}$ in $[\mathbf{P_2W_{18}}]^{6-}$, $[\mathbf{P_2W_{15}}]^{12-}$ and $[\mathbf{P_2W_{12}}]^{12-}$ with those detected in $[\mathbf{P_2W_{17}}]^{10-}$ (set to 100%) gives the approximate amount of the active species $[P^{V}_{2}W^{VI}_{17}O_{61}]^{10-}$ in solution. The so-derived quantities of $[P^{V}_{2}W^{VI}_{17}O_{61}]^{10-}$ (illustrated in Figure 5) increased in the order $[\mathbf{P_2W_{12}}]^{12-}$(~76.9%)<$[\mathbf{P_2W_{15}}]^{12-}$(~82.4%)<$[\mathbf{P_2W_{18}}]^{6-}$(~97.8%)<$[\mathbf{P_2W_{17}}]^{10-}$(100%).

Hydrolysis and rearrangement processes of POMs in aqueous solution occur usually very fast and the newly formed species can be considered as stable. To check the stability of $[P^{V}_{2}W^{VI}_{17}O_{61}]^{10-}$, which was formed in $[\mathbf{P_2W_{18}}]^{6-}$, ^{183}W- and ^{31}P-NMR spectra were recorded on the day of preparation and after 28 days (Figure S11 and S12). The analysis of these spectra shows that it is only the amounts of *α*- and *β*-isomers of the intact Wells-Dawson anion which vary, while the peak intensities for monolacunary $[P^{V}_{2}W^{VI}_{17}O_{61}]^{10-}$ were not changed.

4.4.5. Influence of the substrate *L*-DOPA at pH 6.8 on POT speciation

During the kinetic measurement of $[\mathbf{P_2W_{18}}]^{6-}$, the solution turned blue immediately after addition of *L*-DOPA, hinting towards the reduction of this POT anion[35] in the presence of the substrate (Figure 5). Sadakane *et al.*[36] reported the reduction and protonation from $[P^{V}_{2}W^{VI}_{18}O_{62}]^{6-}$ to $H_2[P^{V}_{2}W^{VI}_{12}W^{V}_{6}O_{62}]^{10-}$ at pH 6.8. Therefore, ^{31}P-NMR (Figure 4) and ^{183}W-NMR (Figure S7, S8, S9) spectra were recorded for $[\mathbf{P_2W_{18}}]^{6-}$, $[\mathbf{P_2W_{15}}]^{12-}$ and $[\mathbf{P_2W_{12}}]^{12-}$ in the presence of 1 mM *L*-DOPA. $[P^{V}_{2}W^{VI}_{17}O_{61}]^{10-}$ was confirmed as the predominant and stable species in $[\mathbf{P_2W_{18}}]^{6-}$ and $[\mathbf{P_2W_{15}}]^{12-}$ in the presence of substrate. The ^{31}P-NMR of $[\mathbf{P_2W_{18}}]^{6-}$ and $[\mathbf{P_2W_{15}}]^{12-}$ showed no significant increase of the free phosphate peaks, which indicated no further decomposition of POT in comparison to substrate-free conditions (Figure 3 and 4) and confirmed $[P^{V}_{2}W^{VI}_{17}O_{61}]^{10-}$ as the most stable species (Figure 5). Interestingly, the decomposition of $[\mathbf{P_2W_{12}}]^{12-}$ with *L*-DOPA at buffer conditions resulted in the rearrangement to $[PW_{11}O_{39}]^{7-}$ (six ^{183}W signals, one

^{31}P-signal, Figures 4 [^{31}P-NMR], S9 [^{183}W-NMR]). No further measurements were undertaken for $[\mathbf{P_2W_{17}}]^{10-}$, as it already exhibits the Wells-Dawson species $[P^{V}_2W^{VI}_{17}O_{61}]^{10-}$ most stable under these conditions, which is the product of rearrangement for the other three Wells-Dawson POTs (summarized in Scheme S1).

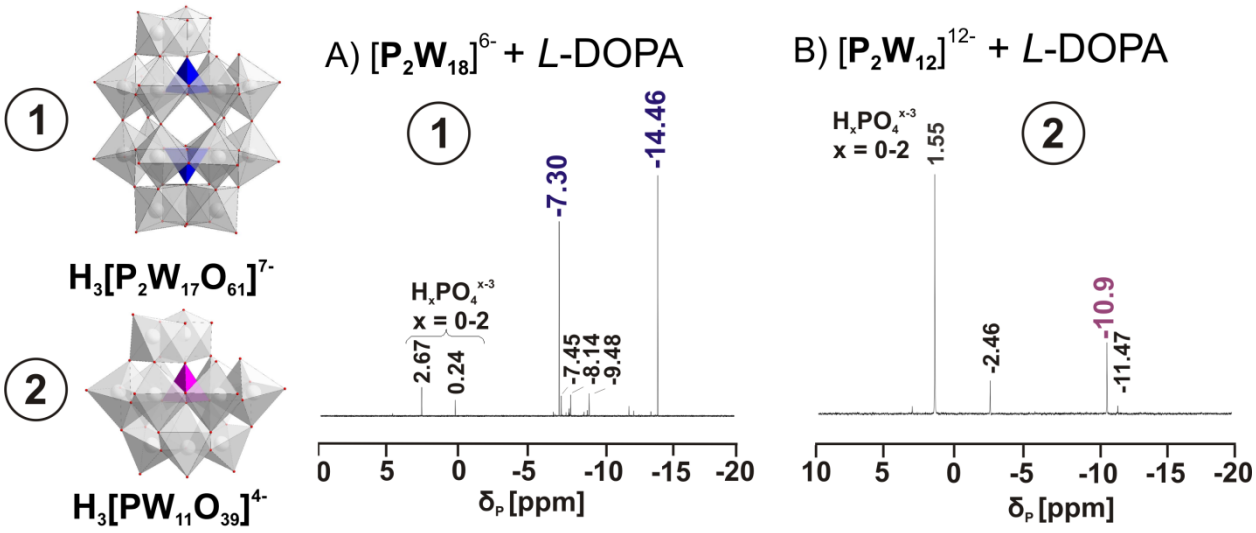

Figure 4. ^{31}P-NMR spectra of $[\mathbf{P_2W_{18}}]^{6-}$ and $[\mathbf{P_2W_{12}}]^{12-}$ at pH 6.8 in the presence of *L*-DOPA. The assignable educts and products of the hydrolytic rearrangement reactions of the respective POTs (approximately 20 mM) under the given buffer conditions are depicted to illustrate the sample speciation. A) product: $H_3[P_2W_{17}O_{61}]^{4-}$; B) product: $H_3[PW_{11}O_{39}]^{4-}$; signal assignment: For A) according to ref. [34], for B) according to ref. [37]. Colour code*:* {WO_6} octahedra, white; {PO_4} tetrahedra, pink, blue; O atoms, red.

4.4.6. Charge density dependence of inhibitory effects of Wells-Dawson POT species

Table 2. Stability at physiological conditions and charge densities (*q/m*) of the Wells-Dawson POTs used. The POT species assigned to observed inhibitory capacity against *ab*PPO4 are depicted in blue.

Educt POT	Charge density *q/m* of POT educt	Stability at pH 6.8	Effective POT		Charge density *q/m* of POT product	
			without *L*-DOPA	in the presence of *L*-DOPA	without *L*-DOPA	in the presence of *L*-DOPA
$[P_2W_{18}O_{62}]^{6-}$	0.33	no	**$H_3[P_2W_{17}O_{61}]^{7-}$**	$H_2[P_2W_{18}O_{62}]^{10-}$	**0.41**	0.56
$[P_2W_{17}O_{61}]^{10-}$	0.59	yes	**$H_3[P_2W_{17}O_{61}]^{7-}$**	**$H_3[P_2W_{17}O_{61}]^{7-}$**	**0.41**	**0.41**
$[P_2W_{15}O_{56}]^{12-}$	0.8	no	**$H_3[P_2W_{17}O_{61}]^{7-}$**	**$H_3[P_2W_{17}O_{61}]^{7-}$**	**0.41**	**0.41**
$H_2[P_2W_{12}O_{48}]^{12-}$	1	no	$H_3[P_2W_{17}O_{61}]^{7-}$	**$H_3[PW_{11}O_{39}]^{4-}$**	0.41	**0.36**

The charge densities for Wells-Dawson clusters were calculated as the ratio between the POT charge *q* and the number of tungsten atoms *m* and summarized in Table 2. For the lacunary Wells-Dawson anion $[P_2W_{17}O_{61}]^{10-}$, which is the main species in $[\mathbf{P_2W_{18}}]^{6-}$, $[\mathbf{P_2W_{17}}]^{10-}$ and $[\mathbf{P_2W_{15}}]^{12-}$ systems, protonation to $H_3[P_2W_{17}O_{61}]^{7-}$ has been reported[38], resulting in a

considerable decrease of the POT charge density (*q/m* = 0.41, Table 2). $[\mathbf{P_2W_{18}}]^{6-}$ (K_i = 9.65) and $[\mathbf{P_2W_{15}}]^{12-}$ (K_i = 13.63) showed lower inhibitory capacities than $[\mathbf{P_2W_{17}}]^{10-}$ (K_i = 6.53) due to their lower content of active $H_3[P_2W_{17}O_{61}]^{7-}$ species. For the $[\mathbf{P_2W_{12}}]^{12-}$ system with *L*-DOPA, the predominating species is the protonated Keggin anion $H_3[PW_{11}O_{39}]^{4-}$ [39]. The similar extent of inhibitory activity of $[\mathbf{P_2W_{17}}]^{10-}$ and $[\mathbf{P_2W_{12}}]^{12-}$ can be explained by the comparable charge densities of the dominating species $H_3[P_2W_{17}O_{61}]^{7-}$ (*q/m* = 0.41) and $H_3[PW_{11}O_{39}]^{4-}$ (*q/m* = 0.36).

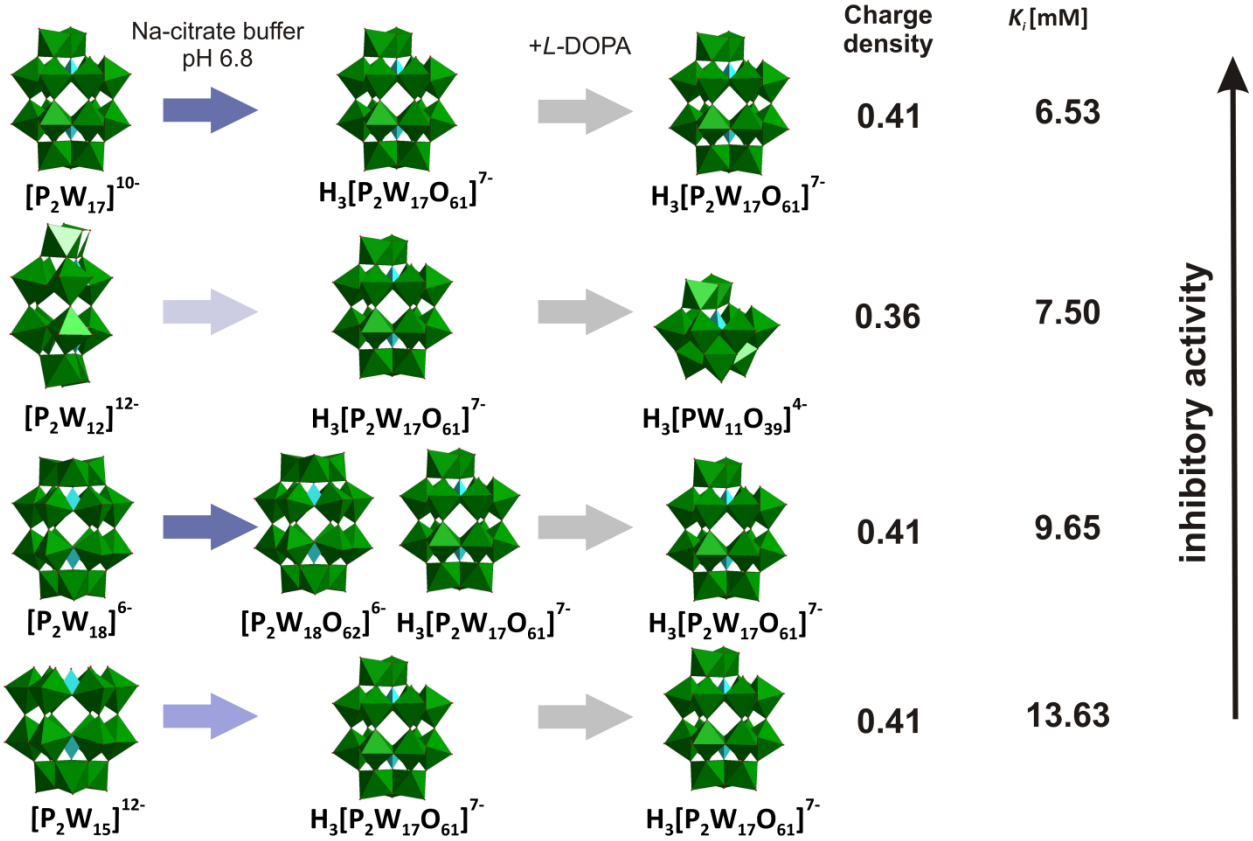

Figure 5. The inhibitory activity of POTs is compared with the main species at pH 6.8 and at assay conditions. The intensity of the violet arrows correlates with the relative rearrangement to $H_3[P_2W_{17}O_{61}]^{7-}$ for the different inhibitors at pH 6.8. The more $H_3[P_2W_{17}O_{61}]^{7-}$ is in the sample, the higher the observed inhibitory activity of the POT. For $[\mathbf{P_2W_{12}}]^{12-}$, the Keggin archetype $H_3[PW_{11}O_{39}]^{4-}$ is the main species at assay conditions, which results in an decrease of the charge density of the POT and in an increase of the inhibitory activity. Colour code*:* {WO_6} octahedra, green; {PO_4} tetrahedra, turquoise.

Notably, the relative amount of the Keggin species as derived from ^{31}P-NMR integration corresponded to only 50.8% of $H_3[P_2W_{17}O_{61}]^{7-}$, but pure $H_3[PW_{11}O_{39}]^{4-}$ demonstrated a weaker inhibition effect on *ab*PPO4 (K_i = 12.0). This supports our previous finding that additional POT species resulting from structural rearrangement processes providing $H_3[PW_{11}O_{39}]^{4-}$ are most likely involved in protein binding.[19] Those anions with a very high charge, such as the trivacant $[\mathbf{P_2W_{15}}]^{12-}$ and hexavacant $[\mathbf{P_2W_{12}}]^{12-}$ Wells-Dawson forms, did not even persist under physiological conditions. Our findings are additionally supported by recent reports about POMs as superchaotrops,[40,41,42] meaning that POMs with intermediate charge density (*q/m* = 0.4) interact considerably strong with various surfaces of different or mixed polarities as presented by a protein molecule[43,44].

4.5. Conclusions

The inhibitory effects of four Wells-Dawson phosphotungstates starting from intact, mono-, three- and hexalacunary forms against *ab*PPO4 were investigated with focus on speciation under the dopochrome assay conditions. During the investigation of $[\mathbf{P_2W_{18}}]^{6-}$, $[\mathbf{P_2W_{17}}]^{10-}$ and $[\mathbf{P_2W_{15}}]^{12-}$, the inhibition effect was assigned to the stable POT species $H_3[P^V_2W^{VI}_{17}O_{61}]^{7-}$, to which $[P^V_2W^{VI}_{18}O_{62}]^{6-}$ and $[P_2W_{15}O_{56}]^{12-}$ rearrange under buffered conditions in significant quantities (>75%) (Figure 5). Interestingly, $[\mathbf{P_2W_{12}}]^{12-}$ was the only system affected by the presence of the substrate *L*-DOPA, as it was converted to the stable active monolacunary Keggin anion $H_3[PW_{11}O_{39}]^{4-}$. The observed order of inhibitory activities is: $[\mathbf{P_2W_{15}}]^{12-}$ (K_i = 13.63) < $[\mathbf{P_2W_{18}}]^{6-}$ (K_i = 9.65) < $[\mathbf{P_2W_{12}}]^{12-}$ (K_i = 7.50) < $[\mathbf{P_2W_{17}}]^{10-}$ (K_i = 6.53) (Figure 5). The magnitude of the inhibitory activities correlated with the amount of $H_3[P_2W_{17}O_{61}]^{7-}$ in the samples, which was quantified by integration of the respective phosphate peaks in the ^{31}P-NMR spectra. The similar inhibitory activity of $[\mathbf{P_2W_{17}}]^{10-}$ and $[\mathbf{P_2W_{12}}]^{12-}$ was explained by the comparable charge densities of the dominating species $H_3[P_2W_{17}O_{61}]^{7-}$ (q/m = 0.41) and $H_3[PW_{11}O_{39}]^{4-}$ (q/m = 0.36), conforming the importance of the charge density for the strength of the inhibitory activity.

4.6. Methods

Protocols for synthesis, spectroscopic assignments and kinetic curves are discussed in the supplementary information. All chemicals have been purchased from Sigma-Aldrich (Vienna, Austria) and Carl-Roth (Karlsruhe, Germany) and were at least of analytical grade. They were used without further purification.

4.6.1. Preparation of *ab*PPO4 in its active form

For the preparation of active *ab*PPO4, the procedure published by Pretzler *et al.*[11] was used. Briefly, latent (inactive) *ab*PPO4 was expressed with an N-terminal gluthathione-S-transferase tag in *E. coli* BL21(DE3). For the protein expression, ZYM-5052 medium[45] without addition of trace elements and with addition of Cu^{2+} [46] was used for 20 h at 20 °C, before 0.5 mM $CuSO_4$ was added to the medium and incubation was continued for further 20 h. The cells were collected in Tris/HCl buffer.

The cell lysis was done via French press. After centrifugation, the supernatant was loaded onto an affinity-chromatography GSTrap Fast Flow column and *ab*PPO4 was yielded after elution with glutathione. The GST tag was cut by digestion with HRV-3C protease. After another affinity-chromatography the inactive latent *ab*PPO4 was obtained in the flow-through. For activation of latent *ab*PPO4 for inhibition studies the C-terminal cap was separated from the PPO with Proteinase K and the activated form was yielded via removal of the C-terminus with size-exclusion chromatography in 50 mM Na-citrate buffer pH 6.8.

4.6.2. Synthesis of α-Wells Dawson POTs

The Wells-Dawson POTs were synthesized according to the procedures given in Table S2 in the Supplementary Information. Slight modifications during the preparations are given below:

1) $(NH_4)_6[P_2W_{18}O_{62}]\cdot 14H_2O$: During the synthesis no bromine water was added.

2) $(NH_4)_{12}[\alpha\text{-}H_2P_2W_{12}O_{48}]\cdot 24H_2O$: The precipitate was collected after reaction overnight.

4.6.3. IR spectroscopy

A Bruker Vertex 70 IR Spectrometer equipped with a single-reflection diamond-ATR unit was used to verify the structure of the applied POTs. The distortion vibrations of W-O-W arise at 400 to 900 cm^{-1}, the W=O stretching vibration occurs in the range of 930-960 cm^{-1} and the P=O vibrations appear between 960-1200 cm^{-1} (Figure S6).

4.6.4. Nuclear magnetic resonance spectroscopy

^{183}W-NMR and ^{31}P-NMR were recorded with a Bruker FT-NMR spectrometer Avance Neo 500 MHz (Bruker, Rheinstetten, Germany) at 25 °C. Chemical shifts were measured relative to 1 M Na_2WO_4 and 85% H_3PO_4. ^{183}W-NMR samples were prepared in 2.7 mL Na-citrate buffer (50 mM, pH 6.8) with POT concentration of 2 mM with or without 1 mM *L*-DOPA and measured in 10 mm tubes. The experimental time was ca. 60 hours, with a standard pulse program at 20.836 MHz and a 63° flip angle with 1s relaxation delay. Subsequently, ^{31}P-NMR was measured at 202.53 MHz.

4.6.5. ^{183}W-NMR

^{183}W-NMR was performed in 50 mM Na-citrate buffer at pH 6.8 to obtain insight into chemical speciation and hydrolytic stability of POTs. The peaks of the ^{183}W-NMR for $[\mathbf{P_2W_{18}}]^{6-}$ are shifted by approx. 4-5 ppm downfield to the assignment in the literature. The slight shifting can be explained by different buffer conditions and ionic strength of solution with regard to the reference data.

The ^{183}W-NMR speciation indicates the presence of $H_3[\alpha_2\text{-}P_2W_{17}O_{61}]^{7-}$ anions in all samples at pH 6.8 (Figure S8, S11). For the ^{183}W-NMR of $[\mathbf{P_2W_{18}}]^{6-}$ at pH 4 two lines (1:2) were assigned (Figure S7), whereas for the same compound at neutral pH a mixture of $[\alpha\text{-}P_2W_{18}O_{62}]^{6-}$ (1:2) and $H_3[\alpha_2\text{-}P_2W_{17}O_{61}]^{7-}$ (2:2:2:2:1:2:2:2:2) was observed (Figure S8). Also, the β-isomer was found at pH 4 and pH 6.8, respectively (Figure S7, S8). Interestingly, the spectra for $[\mathbf{P_2W_{18}}]^{6-}$ at pH 6.8 with *L*-DOPA exhibits only signals for $H_3[\alpha_2\text{-}P_2W_{17}O_{61}]^{7-}$ (Figure S8).

Moreover, in the ^{183}W-NMR spectra for $[\mathbf{P_2W_{12}}]^{12-}$ at buffer conditions signals for $H_3[\alpha_2\text{-}P_2W_{17}O_{61}]^{7-}$ were encountered (Figure S9). In the spectra for $[\mathbf{P_2W_{12}}]^{12-}$ with *L*-DOPA rearrangement to $H_3[\alpha_2\text{-}P_2W_{17}O_{61}]^{7-}$ was detected (Figure S8).

Upon storage of $[P_2W_{18}]^{6-}$ for 28 d, low amounts of the α-isomer, but no β-isomer was detected (Figure S11).

4.6.6. ^{31}P-NMR

The presence of $H_3[P_2W_{17}O_{61}]^{7-}$ in the ^{183}W-NMR at pH 6.8 was confirmed by two respective signals in the ^{31}P-NMR (Figure 3, S10). The signals at 0 or higher ppm values were assigned to $H_xPO_4^{x-3}$ (x = 1, 2), indicating the decomposition of POTs. The signals at -7.3 ppm and -14.46 ppm were assigned to $H_3[P_2W_{17}O_{61}]^7$. The signal at -10.95 ppm in the ^{31}P-NMR of $[\mathbf{P_2W_{12}}]^{12-}$ with substrate corroborated the assignment of $H_3[PW_{11}O_{39}]^{4-}$ from the ^{183}W-NMR (Figure 3).

4.6.7. Electrospray ionization mass spectroscopy

The mass spectrum (Figure S4) was recorded with a LTQ Orbitrap Velos Mass spectrometer (Thermo Fisher Scientific, Bremen, Germany) fitted with a nanospray ion source, coupled to a nano HPLC-system (UltiMate 3000, Dionex), followed by deconvolution with Bruker Compass Software.

The sample was firstly loaded on a µ-Precolumn 5 mm x 300 µ i.d. C4 PepMapp300, 5 µm, 300 Å (Thermo Scientific) with 0.1% TFA. The separation of the sample was implemented on a C4 analytical column 50 cm x 75 µm Accucore C4, 2.6 µm, 150 Å (Thermo Fisher Scientific) at a flow rate of 300 nL/min. Mobile Phase A consisted of 2% ACN, 98% H_2O and 0.1% FA. Mobile Phase B comprised 80% ACN, 20% H_2O and 0.1% FA.

4.6.8. Dopachrome assay

UV-VIS measurements were carried out on a Shimadzu UV 2401PC following the specific absorption of dopachrome at 475 nm (ε = 3700 $M^{-1}cm^{-1}$ 5). For all measurements, 50 mM Na-citrate at pH 6.8 was used as the buffer agent to ensure physiological conditions. The stock solutions of POTs were prepared on the day of measurements and could be used within 3 days.

For a general 1 mL reaction setup in a plastic cuvette, 1 µg/mL *ab*PPO4 was used to catalyze the reaction. The relative inhibition was investigated using 1 mM *L*-DOPA as the substrate and applying an inhibitor concentration range from 0-5 mM to obtain activity curves. For the Lineweaver-Burk plots, an *L*-DOPA concentration range of 0.4-1.5 mM was assayed for three different POT concentrations, respectively.

4.6.9. Acknowledgements

This research was funded by the Austrian Science Fund (FWF): P25217, P27534 and P32326 (to A.R.) and M2203 (to N.G.) and by the University of Vienna, which is gratefully acknowledged. The authors wish to thank Anna Fabisikova, MSc for the ESI-MS measurement.

4.6.10. Author Contributions

Design of the study (R.L., J.B., A.R.); conduction of the study (R.L., J.B., N.G.), data collection, analysis and interpretation (R.L., J.B., N.G., M.G.); Manuscript preparation and review (R.L., J.B., N.G., M.G., A.R.).

4.7. Supplementary information

4.7.1. Structural formulas of *L*-DOPA and kojic acid

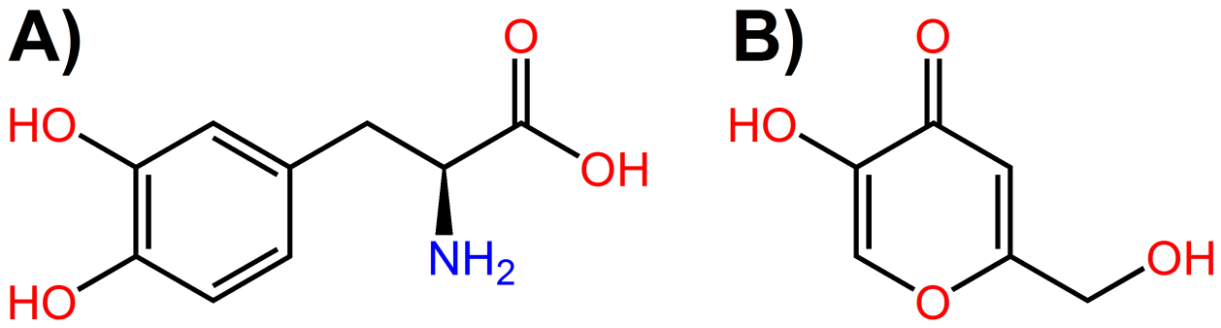

Figure S1. A) *L*-3,4-dihydroxyphenylalanine (*L*-DOPA) was used as substrate assaying the catechol oxidase activity of *ab*PPO4. The diphenol group is oxidized to a quinone[11]. *L*-DOPA was added to $[\mathbf{P_2W_{18}}]^{6-}$, $[\mathbf{P_2W_{15}}]^{12-}$ and $[\mathbf{P_2W_{12}}]^{12}$ for measurements with ^{31}P-NMR and ^{183}W-NMR spectroscopy (Figure 4, S9, S10). B) The competitive inhibitor kojic acid served as a reference compound with known inhibition characteristics in this study.

4.7.2. Characterization of *ab*PPO4

For ESI-MS analysis, the sample was loaded on a trap column µ-Precolumn 5 mm x 300 µ i.d. C4 PepMapp300, 5 µm, 300 Å (Thermo Scientific) with 0.1% TFA. Further separation of the sample from organic molecules and salts was implemented on a C4 analytical column 50 cm x 75 µm Accucore C4, 2.6 µm, 150 Å (Thermo Fisher Scientific) at a flow rate of 300 nL/min. Mobile Phase A consisted of 2% ACN, 98% H_2O and 0.1% FA. Mobile Phase B comprised 80% ACN, 20% H_2O and 0.1% FA. The electrospray voltage was set to 2.1 kV and temperature of the ion transfer capillary was 300 °C. The Full MS scans were gained in positive ion mode at 400-2000 *m/z* range at a resolution of 7500 (FWHM at 400 *m/z*). The mass obtained for the enzyme was 44269 Da (Figure S2).

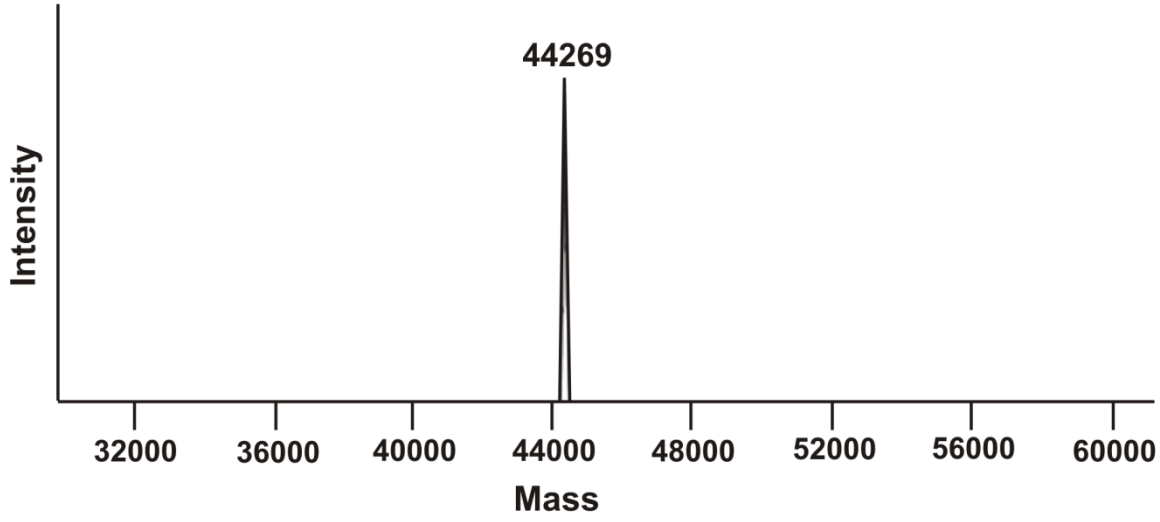

Figure S2. ESI-spectrum (after deconvolution) for active *ab*PPO4 after proteolytic cleavage with Proteinase K.

*Ab*PPO4 contains a vector-derived N-terminal sequence GPLGSPGIP from the protein expression (Figure S3).

GPLGSPGIP

MSLLATVGPT	GGVKNRLDIV	DFVRDEKFFT	LYVRALQAIQ	DKDQADYSSF	FQLSGIHGLP
FTPWAKPKDT	PTVPYESGYC	THSQVLFPTW	HRVYVSIYEQ	VLQEAAKGIA	KKFTVHKKEW
AQAAEDLRQP	YWDTGFALVP	PDEIIKLEQV	KITNYDGTKI	TVRNPILRYS	FHPIDPSFNG
YPNFDTWRTT	VRNPDADKKE	NIPALIAKLD	LEADSTREKT	YNMLKFNANW	EAFSNHGEFD
DTHANSLEAV	HDDIHGFVGR	GAIRGHMTHA	LFAAFDPIFW	LHHSNVDRHL	SLWQALYPGV
WVTQGPEREG	SMGFAPGTEL	NKDSALEPFY	ETEDKPWTSV	PLTDTALLNY	SYPDFDKVKG
GTPDLVRDYI	NDHIDRRYGI	KK			

Figure S3. Protein sequence of *ab*PPO4 after cutting with Proteinase K; green: main domain of the enzyme to lysine (K) 382; violet: histidine (H) at the active center binding the dinuclear copper core; yellow: part of vector sequence[11].

Through the digestion with Proteinase K the peptide sequence GPLGSP was cut from the main peptide sequence and during purification of the tyrosinase glutathione was bound to a cysteine (Table S1). When the ESI-MS was measured under acidic conditions the two copper atoms were lost.

Table S1. The mass of *ab*PPO4 was precisely confirmed by ESI-MS.

Theoretical mass of *ab*PPO4[11][Da]	**Mass of vector amino acids (GPLGSP) [Da]**	**Mass of glutathione [Da]**	**Adduct water [Da]**	**Experimental mass of *ab*PPO4 [Da]**
44451.96	- 526.6	+ 307.3	+ 2 x 18.0	= 44269

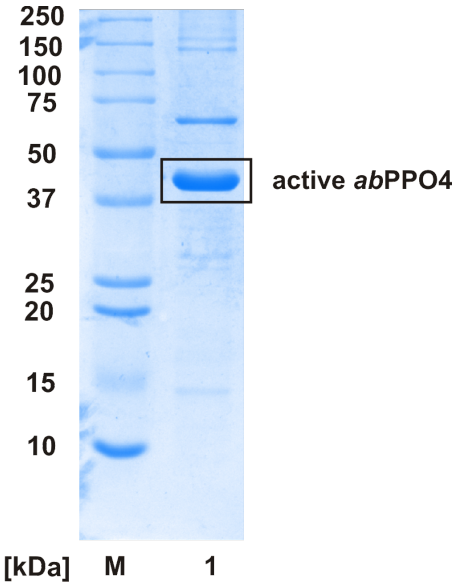

Figure S4. SDS-PAGE of the chromatographic purification of recombinant *ab*PPO4 in its active form according to Pretzler *et al.*[11] For preparation of this figure, the gel was cropped (see Figure S5 for the original image). Lane: M: Precision Plus Protein™ Standard (BIO-RAD), 1: active *ab*PPO4: 44.5 kDa.

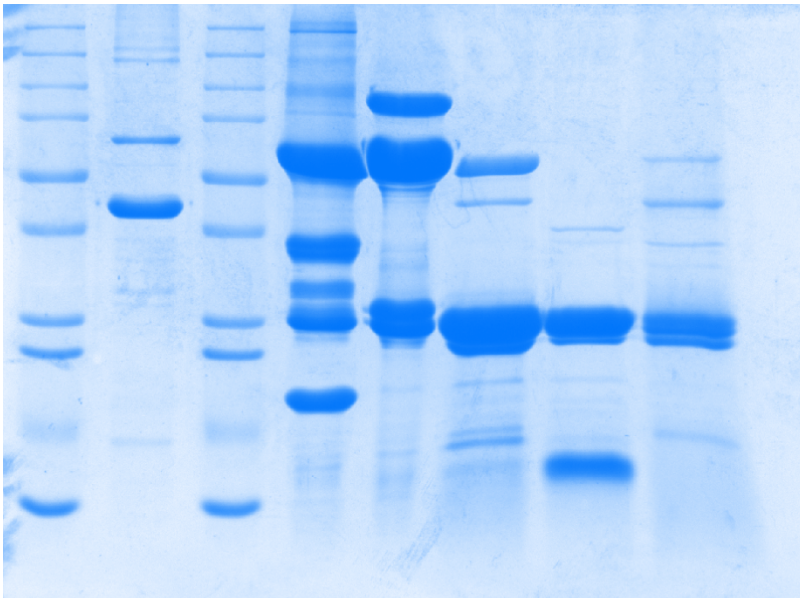

Figure S5. Original gel photography of the SDS-PAGE analysis shown in Figure S4. The image was taken with a Biorad Molecular Imager Gel Doc. The software used was ImageLab (version 5.2.1.) with standard settings for Coomassie-stained SDS-PAGE.

4.7.3. Characterization and NMR-measurements of Wells-Dawson POTs

The Wells-Dawson POTs were analyzed by IR and ^{183}W- and ^{31}P-NMR spectroscopy. The monolacunary Wells-Dawson anion was verified to be the α-isomer[12], (^{183}W-NMR peak intensities: 2:2:2:2:1:2:2:2:2, ^{31}P-NMR: one peak at -13.09 ppm). In $[\mathbf{P_2W_{18}}]^{6-}$ at pH 4 and pH 6.8, a mixture of mostly $[\alpha\text{-}P_2W_{18}O_{62}]^{6-}$ and $[\beta\text{-}P_2W_{18}O_{62}]^{6-}$ (^{183}W-NMR peak intensities: 1:1:2:2,

^{31}P-NMR: two peaks at -11.59 ppm and 12.37 ppm) were revealed. The *β*-isomer is a common byproduct during the synthesis of the α-isomer.[25]

Table S2. Wells-Dawson POTs synthesized in this study and tested for inhibitory activity against *ab*PPO4. Numbered superscripts in brackets demonstrate the assignment of NMR signals to POT species in solution: (1) $[\alpha\text{-}P_2W_{18}O_{62}]^{6-}$, (2) $[\beta\text{-}P_2W_{18}O_{62}]^{6-}$, (3) $[\alpha_2\text{-}P_2W_{17}O_{61}]^{10-}$, (4) $[\alpha\text{-}PW_{11}O_{39}]^{7-}$. The Wells-Dawson POT species are reflected in certain solid state compositions of the studied samples as well. [a] solution pH for NMR spectroscopy, [b] time after solution preparation before NMR measurement, [c] POT first reported by (…), [d] POT synthesis according to (…), [e] assignment according to (…), [f] assignment according to (…).

Wells-Dawson POT	Abbreviation for prepared solution	pH [a]	Time [b]	^{183}W NMR (δ_W) [ppm]	^{31}P NMR (δ_P) [ppm]	Reference			
						1st report [c]	Synthesis [d]	^{31}P NMR [e]	^{183}W NMR [f]
$K_6[\alpha^{(1)}/\beta^{(2)}\text{-}P_2W_{18}O_{62}]\cdot 14\ H_2O$	$[\mathbf{P_2W_{18}}]^{6-}$	6.8	1 d	-107.29$^{(2)}$, -123.61$^{(1)}$, -125.40$^{(3)}$, -129.93$^{(2)}$, -137.77$^{(3)}$, -158.41$^{(3)}$, -166.94$^{(2)}$, -168.82$^{(1)}$, -172.91$^{(3)}$, -178.08$^{(3)}$, -186.42$^{(2)}$, -216.48$^{(3)}$, -218.88$^{(3)}$, -221.27$^{(3)}$, -239.35$^{(3)}$	2.34, 0.00, -7.33$^{(3)}$ -8.29, -11.59$^{(2)}$, -12.37$^{(2)}$, -13.09$^{(1)}$, -14.47$^{(3)}$	24	25	25	47
$K_6[\alpha^{(1)}/\beta^{(2)}\text{-}P_2W_{18}O_{62}]\cdot 14\ H_2O^{(2)}$	$[\mathbf{P_2W_{18}}]^{6-}$	4	1 d	-107.39$^{(2)}$, -123.58$^{(1)}$, -127.12$^{(2)}$, -166.94$^{(2)}$, -168.75$^{(1)}$, -186.34$^{(2)}$	-11.59$^{(2)}$, -12.37$^{(2)}$, -13.09$^{(1)}$	24	25	25	47
$(NH_4)_6[\alpha^{(1)}/\beta^{(2)}\text{-}P_2W_{18}O_{62}]\cdot 14\ H_2O$ + *L*-DOPA	$[\mathbf{P_2W_{18}}]^{6-}$ + *L*-DOPA	6.8	1 d	-125.54$^{(3)}$, -138.04$^{(3)}$, -158.37$^{(3)}$, -173.02$^{(3)}$, -178.31$^{(3)}$, -216.88$^{(3)}$, -219.62$^{(3)}$, -222.03$^{(3)}$, -239.92$^{(3)}$	2.67, 0.24, -7.30$^{(3)}$, -7.45, -8.14, -9.48, -14.46$^{(3)}$	24	25	25	47
$K_6[\alpha^{(1)}/\beta^{(2)}\text{-}P_2W_{18}O_{62}]\cdot 14\ H_2O$	$[\mathbf{P_2W_{18}}]^{6-}$	6.8	28 d	-86.43, -123.79$^{(1)}$, -125.28$^{(3)}$, -137.42$^{(3)}$,	2.39, 0.02, -7.35$^{(3)}$, -7.50,	24	25	25	47

				-158.57[3], -169.09[1], -173.31[3], -177.76[3], -215.73[3], -218.43[3], -220.51[3], -238.59[3]	-8.28, -8.63, -9.99, -13.09, -13.95, -14.44[3]				
$K_{10}[\alpha_2\text{-}P_2W_{17}O_{61}]^{(3)}\cdot 20\ H_2O$	$[\mathbf{P_2W_{17}}]^{10-}$	6.8	1 d	-124.97[3], -137.48[3], -157.58[3], -172.11[3], -177.71[3], -216.03[3], -218.93[3], -221.22[3], -238.81[3]	-7.29[3], -7.82, -8.82, -9.36, -9.86, -14.47[3]	26	25	25	47
$K_{12}[\alpha\text{-}P_2W_{15}O_{56}]\cdot 24\ H_2O$	$[\mathbf{P_2W_{15}}]^{12-}$	6.8	1 d	-124.97[3], -137.46[3], -157.58[3], -172.11[3], -177.71[3], -216.09[3], -218.93[3], -222.71[3], -238.71[3]	3.01, 0.99, -7.30[3], -9.38, -14.46[3]	27	25	25	47
$K_{12}[\alpha\text{-}P_2W_{15}O_{56}]\cdot 24\ H_2O$ + *L*-DOPA	$[\mathbf{P_2W_{15}}]^{12-}$ + *L*-DOPA	6.8	1 d	(not performed due to clarification by ^{31}P-NMR)	4.35, 2.41, -7.25[3], -8.04, -14.42[3]	27	25	25	47
$(NH_4)_{12}[\alpha\text{-}H_2P_2W_{12}O_{48}]\cdot 24\ H_2O$	$[\mathbf{P_2W_{12}}]^{12-}$	6.8	1 d	-82.77, -125.39[3], -137.57[3], -158.32[3], -172.49[3], -177.69[3], -216.36[3], -218.71[3], -221.23[3], -239.17[3]	2.71, 0.18, -7.32[3], -7.74, -9.81, -10.93, -14.47[3]	29	25	25	47
$(NH_4)_{12}[\alpha\text{-}H_2P_2W_{12}O_{48}]\cdot 24\ H_2O$ + *L*-DOPA	$[\mathbf{P_2W_{12}}]^{12-}$ + *L*-DOPA	6.8	1 d	-68.37[4], -96.10[4], -107.95[4], -130.95[4], -139.24[4], -152.05[4]	1.55, -2.46, -10.95[4], -11.47	29	48	37	37

4.7.3.1. IR spectroscopy

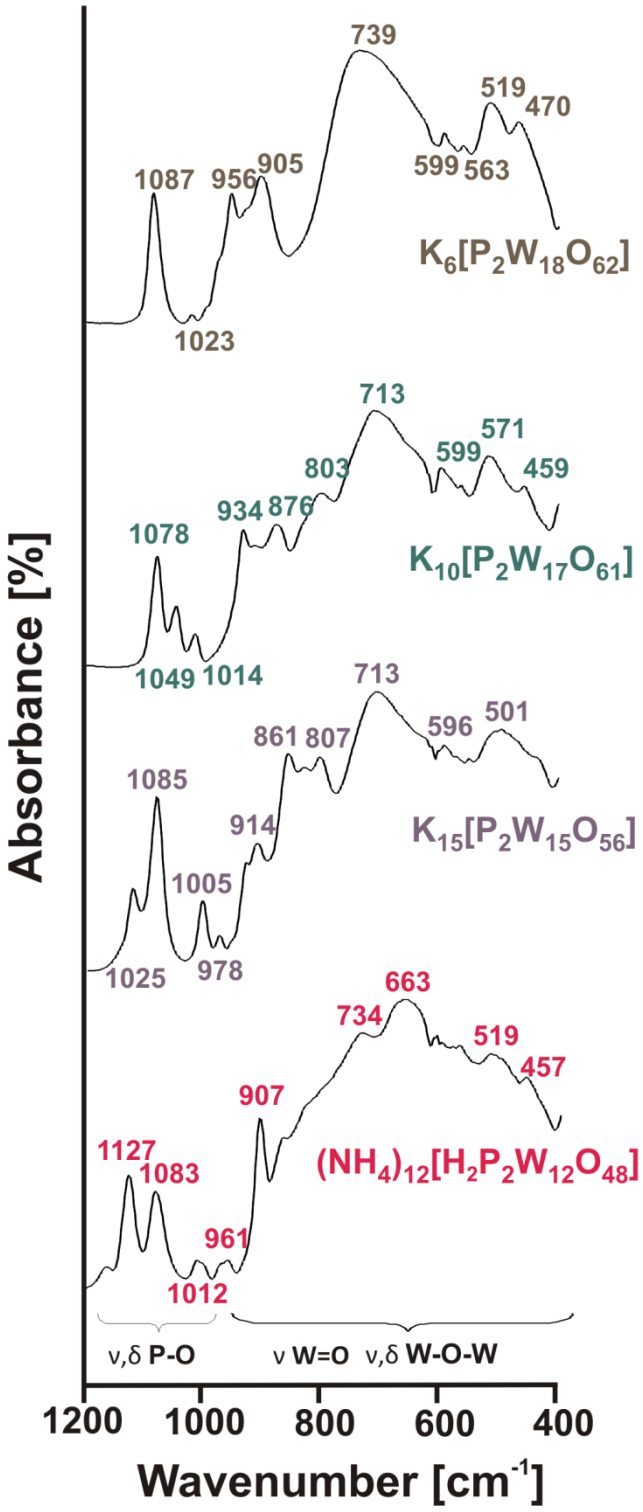

Figure S6. IR spectra of the Wells-Dawson POTs used in this study in the region of W-O-W, W-O-P and W=O bonds vibrations (1200 – 400 cm^{-1}).

4.7.3.2. ^{183}W-NMR

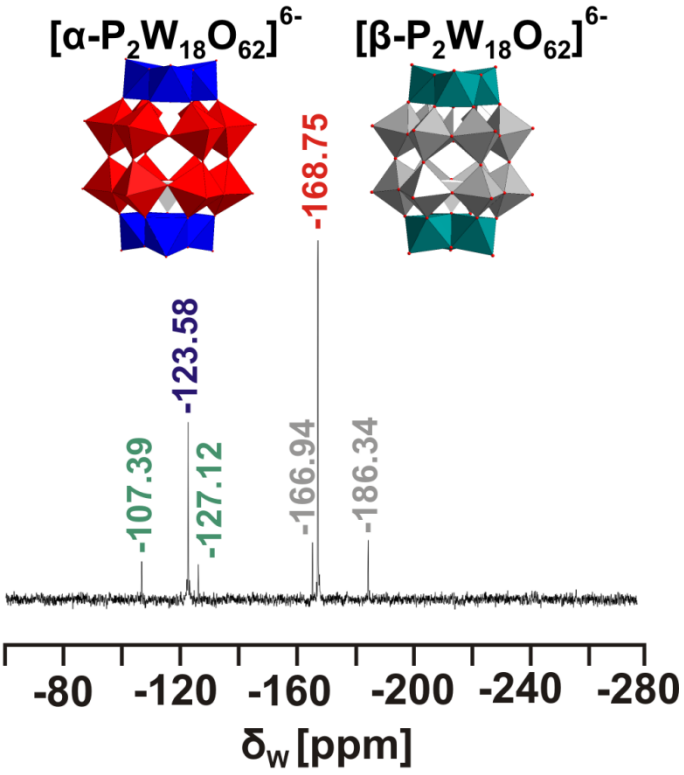

Figure S7. ^{183}W-NMR of $[\mathbf{P_2W_{18}}]^{6-}$ at pH 4 (Table S2). Signal assignment according to ref.[47]. $[\alpha\text{-}P_2W_{18}O_{62}]^{6-}$ and $[\beta\text{-}P_2W_{18}O_{62}]^{6-}$ could be confirmed as stable at pH 4 as suggested by the literature (ref. [24]). *Colour code*: $[\alpha\text{-}P_2W_{18}O_{62}]^{6-}$: cap of $\{WO_6\}$ octahedra, blue; belt of $\{WO_6\}$ octahedra, red; $[\beta\text{-}P_2W_{18}O_{62}]^{6-}$: cap of $\{WO_6\}$ octahedra, petrol; belt of $\{WO_6\}$ octahedra, grey; $\{PO_4\}$ tetrahedron, white.

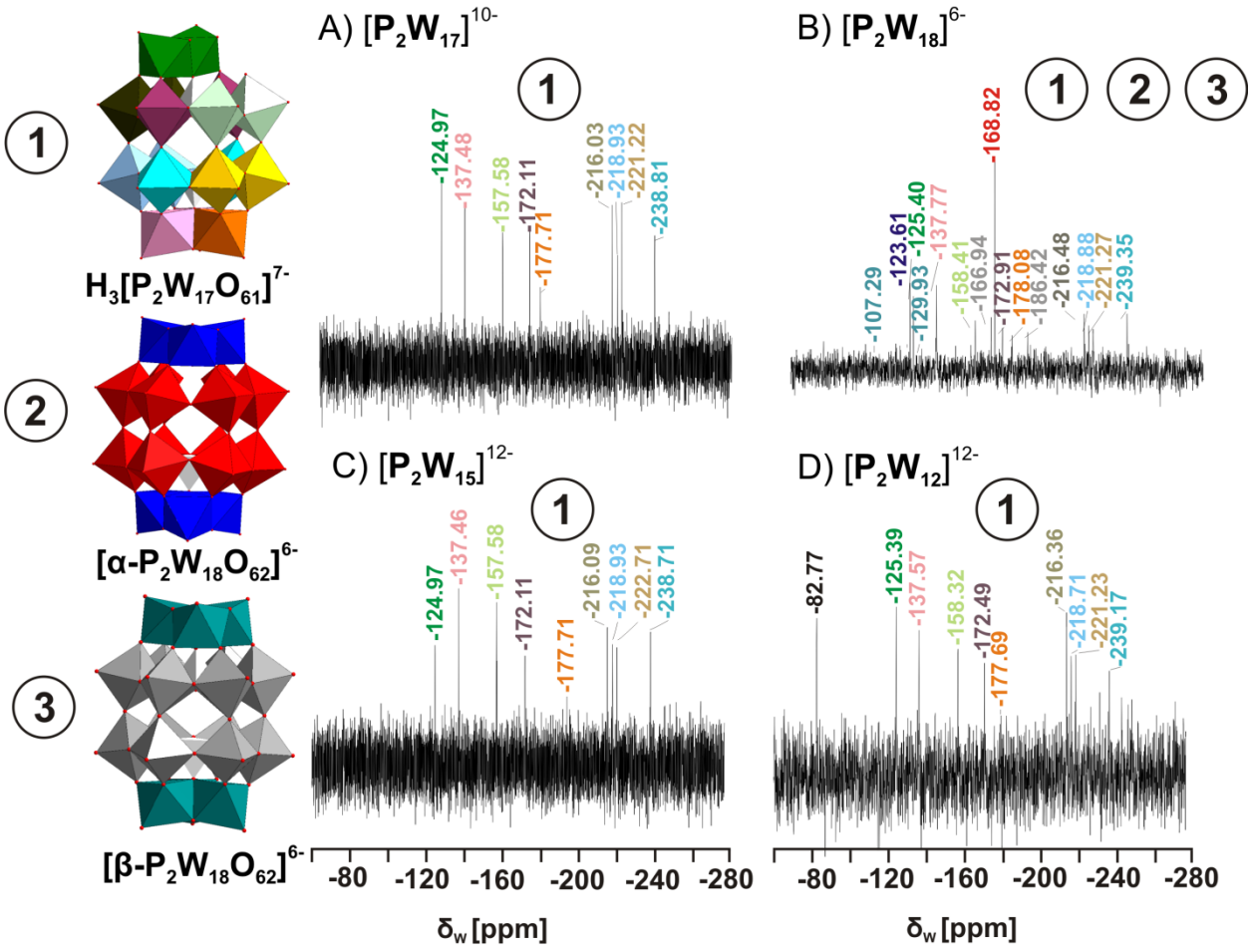

Figure S8. ^{183}W-NMR spectra of $[\mathbf{P_2W_{18}}]^{6-}$, $[\mathbf{P_2W_{17}}]^{10-}$, $[\mathbf{P_2W_{15}}]^{12-}$ and $[\mathbf{P_2W_{12}}]^{12-}$ at pH 6.8 (Table S2). The assignable educts and products of the hydrolytic rearrangement reactions of the respective POTs under the given buffer conditions are depicted to illustrate the sample speciation. A) educt/product: $H_3[P_2W_{17}O_{61}]^{7-}$; B) educts: $[\alpha\text{-}P_2W_{18}O_{62}]^{6-}$ and $[\beta\text{-}P_2W_{18}O_{62}]^{6-}$, product: $H_3[P_2W_{17}O_{61}]^{7-}$; C) product: $H_3[P_2W_{17}O_{61}]^{7-}$; D) product: $H_3[P_2W_{17}O_{61}]^{7-}$. Signal assignment according to ref.[47]. Rearrangement to $H_3[P_2W_{17}O_{61}]^{7-}$ was observed in all cases. *Colour code*: $[\alpha\text{-}P_2W_{18}O_{62}]^{6-}$: cap of $\{WO_6\}$ octahedra, blue; belt of $\{WO_6\}$ octahedra, red; $[\beta\text{-}P_2W_{18}O_{62}]^{6-}$: cap of $\{WO_6\}$ octahedra, petrol; belt of $\{WO_6\}$ octahedra, grey. $H_3[P_2W_{17}O_{61}]^{7-}$ $\{WO_6\}$ octahedra: top, olive green; upper belt left, dark grey; upper belt middle, lavender; upper belt right, light green; lower belt left, light blue; lower belt middle, turquoise; lower belt right, gold; bottom left, pink; bottom right, orange; $\{PO_4\}$ tetrahedra, white.

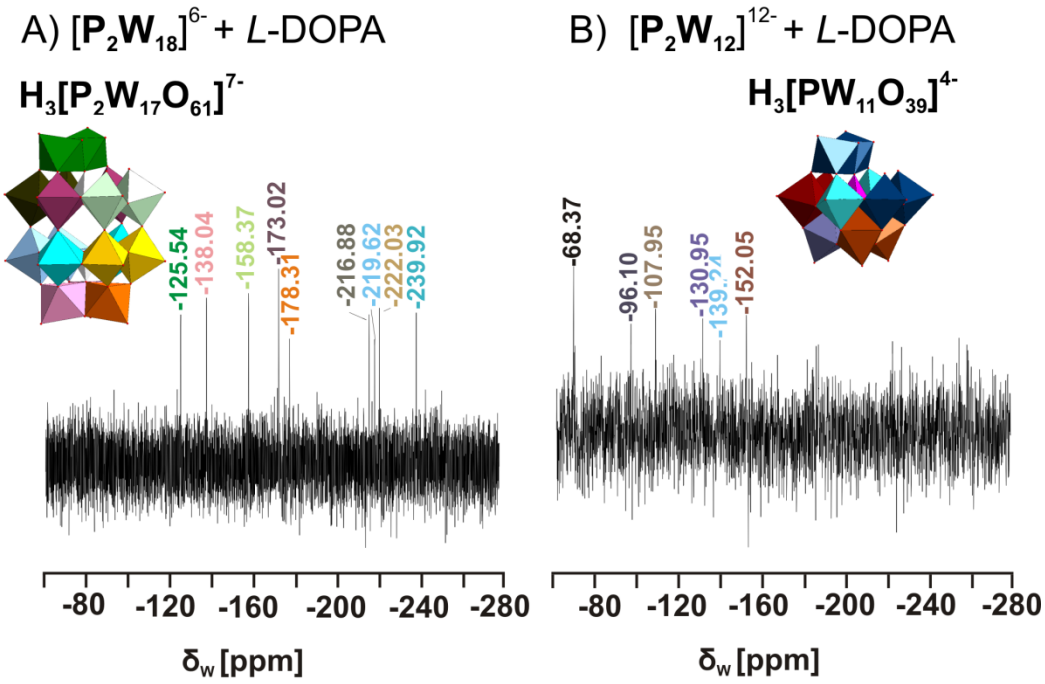

Figure S9. ^{183}W-NMR spectra of $[\mathbf{P_2W_{18}}]^{6-}$ and $[\mathbf{P_2W_{12}}]^{12-}$ in the presence of *L*-DOPA at pH 6.8 (Table S2). The assignable educts and products of the hydrolytic rearrangement reactions of the respective POTs under the given buffer conditions are depicted to illustrate the sample speciation. A) product: $H_3[P_2W_{17}O_{61}]^{7-}$; B) product: $H_3[PW_{11}O_{39}]^{4-}$; Signal assignment: for A) according to ref.[47]; for B) according to ref.[37]. Rearrangement to $H_3[P_2W_{17}O_{61}]^{7-}$ was observed in A), and rearrangement to $H_3[PW_{11}O_{39}]^{4-}$ was observed in B). *Colour code*: $H_3[P_2W_{17}O_{61}]^{7-}$ $\{WO_6\}$ octahedra: top, olive green; upper belt left, dark grey; upper belt middle, lavender; upper belt right, light green; lower belt left, light blue; lower belt middle, turquoise; lower belt right, gold; bottom left, pink; bottom right, orange; $\{PO_4\}$ tetrahedron, white. $H_3[PW_{11}O_{39}]^{4-}$ $\{WO_6\}$ octahedra: top and belt right, dark petrol; belt middle, light blue; belt left, dark red; bottom left, violet; bottom right, brown; $\{PO_4\}$ tetrahedron, purple.

4.7.3.3. ^{31}P-NMR

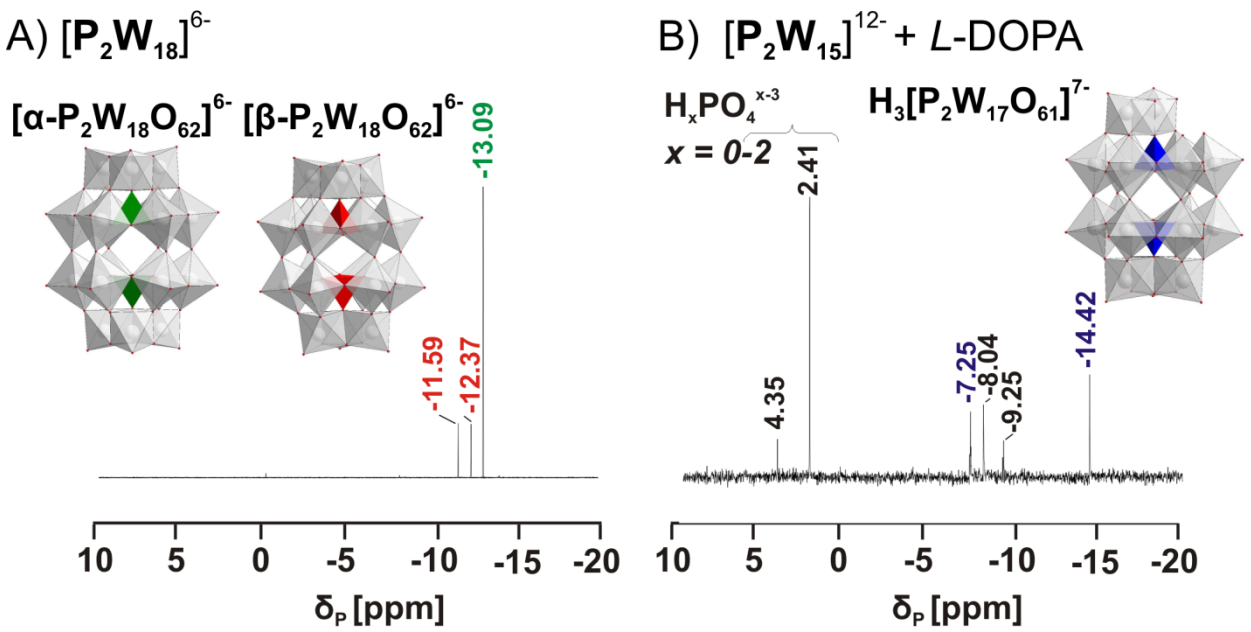

Figure S10. ^{31}P-NMR of $[\mathbf{P_2W_{18}}]^{6-}$ at pH 4 and $[\mathbf{P_2W_{15}}]^{12-}$ + *L*-DOPA at pH 6.8 (Table S2). Signal assignment for A) according to ref.[25] and for B) according to ref.[37]. A) [α-$\mathbf{P_2W_{18}}$]$^{6-}$ and [**β-P$_2$W$_{18}$**]$^{6-}$ were verified as proposed by the literature (ref. [25]). B) Most of $[\mathbf{P_2W_{15}}]^{12-}$ rearranged towards $[\mathbf{P_2W_{17}}]^{10-}$ under release of free phosphate. *Colour code:* {WO_6} octahedral, white; {PO_4} tetrahedral in [α-$P_2W_{18}O_{62}$]$^{6-}$, green; {PO_4} tetrahedra in [β-$P_2W_{18}O_{62}$]$^{6-}$, red; {PO_4} tetrahedra in $H_3[P_2W_{17}O_{61}]^{7-}$, blue.

4.7.3.4. Long term stability of $[P_2W_{18}]^{6-}$ determined by ^{183}W-NMR and ^{31}P-NMR

To explore the long term stability of Wells-Dawson POTs, the sample composition was analyzed after 4 weeks of storage at room temperature. ^{183}W-NMR and ^{31}P-NMR were measured for $[\mathbf{P_2W_{18}}]^{6-}$ at pH 6.8. After 28 days, a decrease of $[\alpha\text{-}P_2W_{18}O_{61}]^{6-}$ as well as the disappearance of $[\beta\text{-}P_2W_{18}O_{61}]^{6-}$ could be observed. Furthermore, a slight increase in the phosphate peak was found, which indicated more decomposition of POT. All the other NMR measurements in this study were carried out after one day.

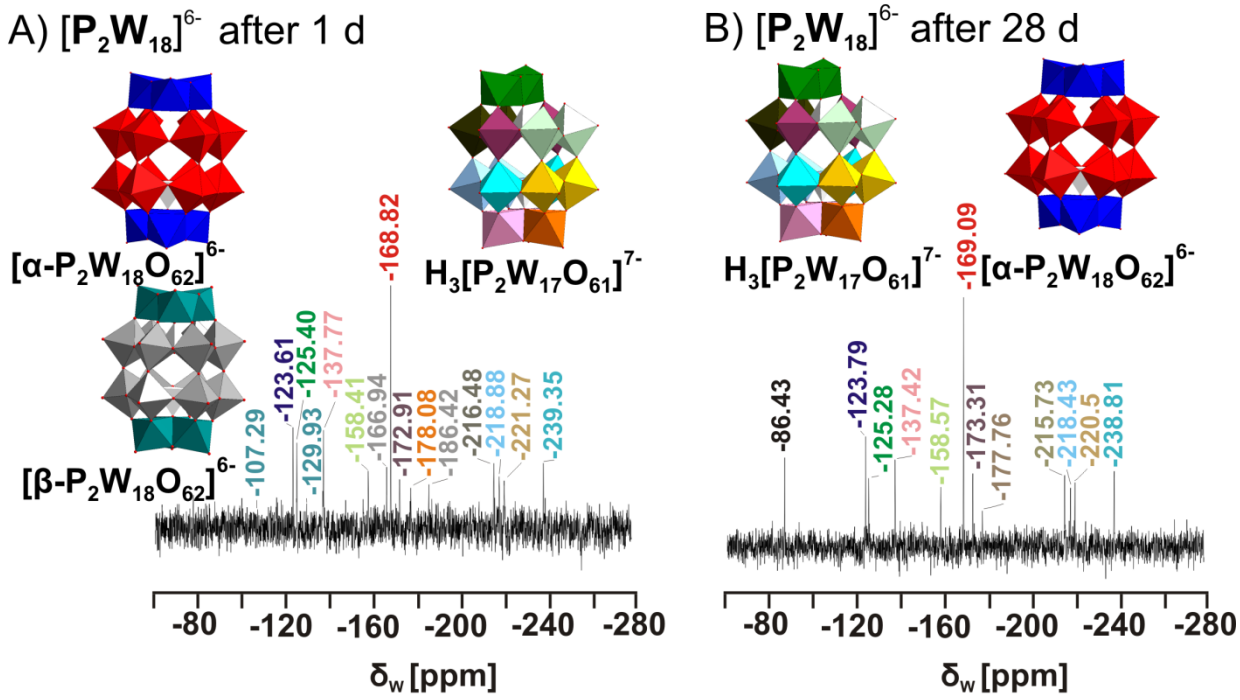

Figure S11. ^{183}W-NMR spectra of $[\mathbf{P_2W_{18}}]^{6-}$ after 28 d, at pH 6.8 (Table S2). Signal assignment: for A) according to ref.[47]. A) educts: $[\alpha\text{-}P_2W_{18}O_{62}]^{6-}$ and $[\beta\text{-}P_2W_{18}O_{62}]^{6-}$, product: $H_3[P_2W_{17}O_{61}]^{7-}$. B) educt/product: $[P_2W_{18}O_{62}]^{6-}$, product: $H_3[P_2W_{17}O_{61}]^{7-}$. In comparison to the measurement after 1 d, complete transformation of $[\beta\text{-}P_2W_{18}O_{62}]^{6-}$ to the α-form was discovered as the loss of corresponding signals in the spectrum. *Colour code*: $[\alpha\text{-}P_2W_{18}O_{62}]^{6-}$: cap of $\{WO_6\}$ octahedra, blue; belt of $\{WO_6\}$ octahedra, red; $[\beta\text{-}P_2W_{18}O_{62}]^{6-}$: cap of $\{WO_6\}$ octahedra, petrol; belt of $\{WO_6\}$ octahedra, grey. $H_3[P_2W_{17}O_{61}]^{7-}$ $\{WO_6\}$ octahedra: top, olive green; upper belt left, dark grey; upper belt middle, lavender; upper belt right, light green; lower belt left, light blue; lower belt middle, turquoise; lower belt right, gold; bottom left, pink; bottom right, orange; $\{PO_4\}$ tetrahedra, white.

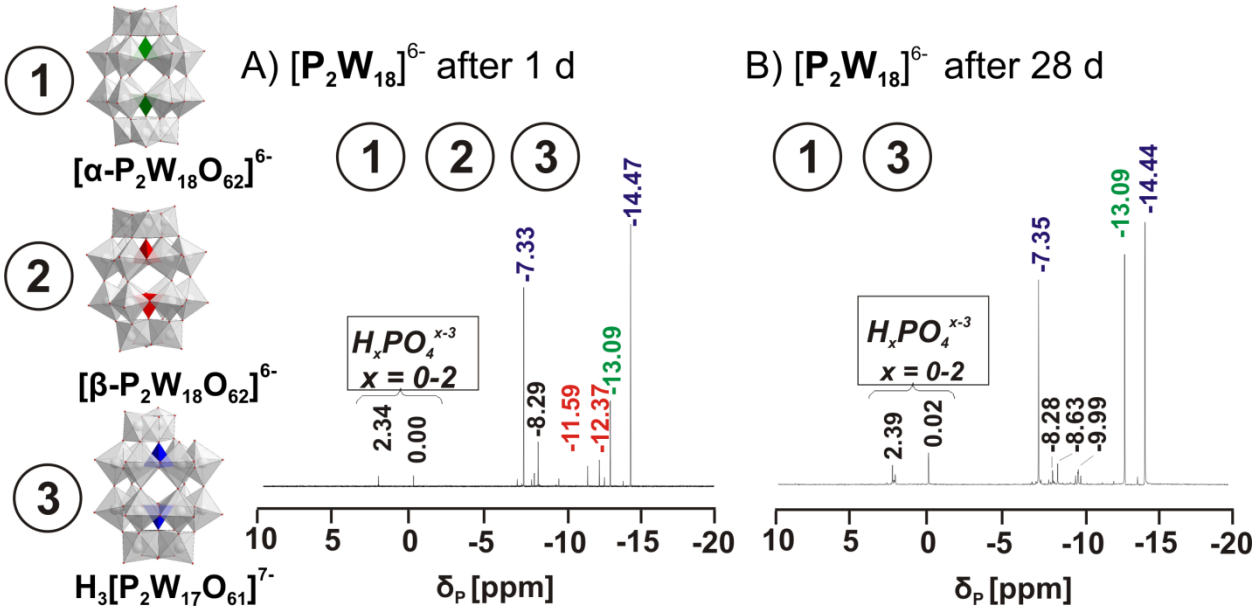

Figure S12. ^{31}P-NMR - of $[\mathbf{P_2W_{18}}]^{6-}$ after 1 d and 28 d, at pH 6.8 (Table S2). Signal assignment according to ref.[25,37]. A) educts: $[\alpha\text{-}P_2W_{18}O_{62}]^{6-}$ and $[\beta\text{-}P_2W_{18}O_{62}]^{6-}$, product: $H_3[P_2W_{17}O_{61}]^{7-}$. B) educt/product: $[\alpha\text{-}P_2W_{18}O_{62}]^{6-}$, product: $H_3[P_2W_{17}O_{61}]^{7-}$. In comparison to the measurement after 1 d, an extinction of signals for $[\beta\text{-}P_2W_{18}O_{62}]^{6-}$ was discovered, demonstrating complete conversion to the α-form. *Colour code:* $\{WO_6\}$ octahedra, white; $\{PO_4\}$ tetrahedra in $[\alpha\text{-}P_2W_{18}O_{62}]^{6-}$, green; $\{PO_4\}$ tetrahedra in $[\beta\text{-}P_2W_{18}O_{62}]^{6-}$, red; $\{PO_4\}$ tetrahedra in $H_3[P_2W_{17}O_{61}]^{7-}$, blue.

4.7.4. Comprehension of structural POT rearrangements

The rearrangement processes at pH 6.8 for the Wells-Dawson POTs under study identified by ^{31}P- and ^{183}W-NMR analysis in the preceeding sections are illustrated in Scheme S1:

$$17\ [P_2W_{18}O_{62}]^{6-} + 2\ HPO_4^{2-} + 74\ OH^- \longrightarrow 18\ [P_2W_{17}O_{61}]^{10-} + 38\ H_2O \quad (1)$$

$$17\ [P_2W_{15}O_{56}]^{12-} + 46\ H^+ \longrightarrow 15\ [P_2W_{17}O_{61}]^{10-} + 4\ HPO_4^{2-} + 21\ H_2O \quad (2)$$

$$17\ [H_2P_2W_{12}O_{48}]^{12-} + 64\ H^+ \longrightarrow 12\ [P_2W_{17}O_{61}]^{10-} + 10\ HPO_4^{2-} + 44\ H_2O \quad (3)$$

$$11\ [H_2P_2W_{12}O_{48}]^{12-} + 28\ H^+ \longrightarrow 12\ [PW_{11}O_{39}]^{7-} + 10\ HPO_4^{2-} + 20\ H_2O \quad (4)$$

Scheme S1: Proposed chemical equations for the structural interconversions observed in buffered solutions of Wells-Dawson POTs at pH 6.8 without *L*-DOPA ((1) – (3)) and in the presence of L-DOPA ((4)). HPO_4^{2-} was chosen as the dominating phosphate form at neutral pH, and the protonation of POT anions was neglected for simplification. However, the degree of protonation does not affect the structural scaffolds illustrated here.

4.7.5. Summary of POT charge densities of Keggin and Wells-Dawson POTs

In order to facilitate comparison of the inhibitory capacities of the Keggin and Wells-Dawson POT samples tested in our laboratory against *ab*PPO4 and to obtain a structure-activity correlation, the charge densities (anionic charge per W addenda atom) of the species present before and after solubilization in physiological buffer were arranged in Table S3. With regard to the charge densities, the following stability windows for POTs can be identified:

1) intact closed clusters: $q/m \approx 0.33 – 0.50$

Structures with higher charge densities were not analyzed. Structures with a *q/m* value lower than 0.33 tend to hydrolysis or reduction under suitable conditions, both leading to an increase in charge density.

2) lacunary clusters: $q/m = 0.36 – 0.45$

Structures with lower charge densities were not analyzed. Structures with a *q/m* value higher than 0.45 achieve stabilization by taking up protons for charge compensation. However, too highly charged anions decompose and rearrange to more stable solution structures. Both of these pathways result in a decrease in charge density.

Overall, the preferred stable charge densities at neutral pH of both the intact and lacunary POTs investigated took values close to 0.4, and higher charge densities were only revealed as stable for intact clusters. This seems to be an intrinsic POT property as a combined result of 1) the reactivity of lacunary oxygen sites and 2) the hydrolytic susceptibility to hydroxide anions in aqueous solution in competition with electrostatic repulsion with the anionic POT charge. Notably, the size of the POT cluster does not play a role for these effects concerning single metal centers in their oxygen-bound environment.

The scenario is different when looking at the POT interaction with the enzyme *ab*PPO4. Among the same-sized Keggin compounds exhibiting inhibitory effects on the enzyme, the apparent K_i values show a clear correlation to the *q/m* values, with the lowest charge density corresponding to the highest protein affinity. But going to the larger Wells-Dawson archetype, comparing the active lacunary species $H_3[PW_{11}O_{39}]^{4-}$ (Keggin) and $H_3[P_2W_{17}O_{61}]^{7-}$ (Wells-Dawson), higher protein affinities were observed for the bigger cluster despite of slightly higher charge densities. As stated in the main text, the basic inhibition effect shown by the Wells-Dawson clusters was revealed to correlate to the amount of the protein-binding species $H_3[P_2W_{17}O_{61}]^{7-}$ present in solution. The observed inhibition effect for the POT sample $[\mathbf{P_2W_{12}}]^{12-}$ appears to be caused by two lacunary species with suitable charge density.

Table S3: Summary of Keggin and Wells-Dawson POT speciation from two studies. The speciation of various Keggin POTs was taken from [19], the speciation of Wells-Dawson POTs is the result of the present study. The POT compounds (educts) undergo different structural changes upon dissolution in 50 mM Na-citrate pH 6.8 to form species (products) most stable under these conditions. Colour code: orange, not stable; yellow, partially stable; light green, stabilized by protonation; green, stable; blue, obtained under long-term reducing conditions (3 days) in the presence of 1 mM L-DOPA. The POT species assigned to observed inhibitory capacity against *ab*PPO4 are depicted in italics. It becomes obvious that POT species with a charge density close to 0.4 dominate at neutral pH and interact most strongly with the enzyme.

POT educt	Charge density *q/m*	Stability at pH 6.8	Reaction to achieve stabilization		POT product(s)		Charge density *q/m*		K_i [mM]
$[PW_{12}O_{40}]^{3-}$	0.25	no	hydrolysis		*$H_3[PW_{11}O_{39}]^{4-}$*		*0.36*		25.6
$[PW_{11}O_{39}]^{7-}$	0.64	yes	protonation		*$H_3[PW_{11}O_{39}]^{4-}$*		*0.36*		12.0
$[SiW_{12}O_{40}]^{4-}$	0.33	partial	-	hydrolysis	*$[SiW_{12}O_{40}]^{4-}$*	$H_3[SiW_{11}O_{39}]^{5-}$	*0.33*	0.45	4.7
$[SiW_{11}O_{39}]^{8-}$	0.73	yes	protonation		$H_3[SiW_{11}O_{39}]^{5-}$		0.45		-
$[BW_{12}O_{40}]^{5-}$	0.42	yes	-		-		-		-
$[AlW_{12}O_{40}]^{5-}$	0.42	yes	-		-		-		-
$[AlW_{11}O_{39}]^{9-}$	0.82	no	rearrangement		*$[AlW_{11}O_{39}\{Al(H_2O)\}]^{6-}$*		*0.50*		54.1
$[H_2W_{12}O_{40}]^{6-}$	0.50	yes	-		-		-		-
$[BeW_{12}O_{40}]^{6-}$	0.50	yes	-		-		-		-
$[P_2W_{18}O_{62}]^{6-}$	0.33	no	hydrolysis	reduction	*$H_3[P_2W_{17}O_{61}]^{7-}$*	$H_2[P_2W_{18}O_{62}]^{10-}$	*0.41*	0.56	9.7
$[P_2W_{17}O_{61}]^{10-}$	0.59	yes	protonation		*$H_3[P_2W_{17}O_{61}]^{7-}$*		*0.41*		6.5
$[P_2W_{15}O_{56}]^{12-}$	0.80	no	rearrangement		*$H_3[P_2W_{17}O_{61}]^{7-}$*		*0.41*		13.6
$H_2[P_2W_{12}O_{48}]^{12-}$	1.00	no	rearrangement		*$H_3[P_2W_{17}O_{61}]^{7-}$*	*$H_3[PW_{11}O_{39}]^{4-}$*	*0.41*	*0.36*	7.5

4.7.6. Hyperbolic activity curve fit

Copeland *et al.*[30] presented the hyberbolic curve fit for enzymatic activity based on the Michaelis-Menten equation (1), which is

$$v = v_{max} \frac{[S]}{K_M + [S]}. \quad (1)$$

v is the enzymatic reaction velocity, v_{max} the maximal enzymatic velocity of the enzyme, K_M the concentration of the half-maximal velocity and $[S]$ the substrate concentration. If enzyme inhibition is taken into account, apparent values (e.g. v_{app}, $v_{max,app}$, $K_{M,app}$) are employed. For all inhibition mechanisms the apparent maximal velocity $v_{max,app}$ is given by

$$v_{max,app} = \frac{v_{max}}{1 + \frac{[I]}{\alpha K_i}} \quad (2)$$

and the apparent Michalis-Menten constant $K_{M,app}$ is

$$K_{M,app} = \frac{K_M(1 + \frac{[I]}{K_i})}{1 + \frac{[I]}{\alpha K_i}} \quad (3)$$

Expressions (1) and (2) are inserted into equation (3). To obtain the relative inhibition (in %), v_{app} is divided by the uninhibited enzymatic velocity v.

$$\frac{v_{app}}{v} = 100 \frac{K_M + [S]}{K_M\left(1 + \frac{[I]}{K_i}\right) + [S]\left(1 + \frac{[I]}{\alpha K_i}\right)} \quad (4)$$

The concentration of *L*-DOPA was kept constant at 1 mM for all experiments. As determined by Pretzler et al.**Fehler! Textmarke nicht definiert.**, K_M was set to 26.1 mM. The final hyberbolic equation (5) was used for the curve fit with OriginPro 8:

$$\frac{v_{app}}{v} = 100 \frac{27.1}{27.1 + \left(\frac{26.1 + \frac{1}{\alpha}}{K_i}\right)[I]}. \quad (5)$$

The initial parameters for the regression were taken from the Lineweaver-Burk plots as described in Section 4.7.8.

4.7.7. Curve fit via algorithm with Dr-Fit software

To investigate the underlying inhibition processes in more detail (*e.g.* multiple stimulatory or inhibitory effects), a multiphasic model was employed to fit the data. Therefore, an algorithm implemented in the Dr-Fit software (https://sourceforge.net/projects/drfit/) was used for modeling[49]. The basic mathematical entity of the program is the Hill model based on equation

$$E_{Hill}(C; E_\infty, E_0, EC_{50}, H) = E_0 + \frac{E_\infty - E_0}{1 + \left(\frac{EC_{50}}{C}\right)^H}. \quad (6)$$

The EC_{50} value is the concentration at half-maximal effect, E_0 is the effect if no inhibitor is present, H is the Hill exponent, E_∞ is the maximal effect, E_{Hill} is the resulting effect from the Hill equation and C is the concentration.

For a system with multiphasic inhibition (*e.g.* points of inflection in the curves, connected agonist and antagonist effects), a simple Hill equation does not properly describe the complex binding behavior between enzyme and inhibitor. For this reason, an extended model is introduced, where each phase is considered as a part of a consecutive reaction to yield the total effect $E(C)$. It can be obtained as the product of the effect of every partial process $E_i(C)$.

$$E(C) = \Pi_i^n E_i(C) \quad (7)$$

$E_i(C)$ is written,

$$E_i(C; E_{\infty i}, EC_{50i}, H_i) = 1 + \frac{E_{\infty i} - 1}{1 + \left(\frac{EC_{50i}}{C}\right)^{H_i}} \quad (8)$$

The general equation is,

$$E(C; E_{\infty i} \dots E_{\infty n}, EC_{50i} \dots EC_{50n}, H_i \dots H_n) = \Pi_i^n \left(1 + \frac{E_{\infty i} - 1}{1 + \left(\frac{EC_{50i}}{C}\right)^{H_i}}\right) \quad (9)$$

Although there is no theoretical limit, in the software the case with $n = 3$ is applied, which proved to be suitable to explain most experimental data. It is

$$E(C) = \left(1 + \frac{E_{\infty\,1} - 1}{1 + \left(\frac{EC_{50\,1}}{C}\right)^{H_1}}\right)\left(1 + \frac{E_{\infty\,2} - 1}{1 + \left(\frac{EC_{50\,2}}{C}\right)^{H_2}}\right)\left(1 + \frac{E_{\infty\,3} - 1}{1 + \left(\frac{EC_{50\,3}}{C}\right)^{H_3}}\right) \quad (10)$$

To obtain the relative effect as the final fitting equation, it has to be divided by E_{max}:

$$\frac{E(C)}{E_{max}} = \left(1 + \frac{E_{\infty\,1} - 1}{1 + \left(\frac{EC_{50\,1}}{C}\right)^{H_1}}\right)\left(1 + \frac{E_{\infty\,2} - 1}{1 + \left(\frac{EC_{50\,2}}{C}\right)^{H_2}}\right)\left(1 + \frac{E_{\infty\,3} - 1}{1 + \left(\frac{EC_{50\,3}}{C}\right)^{H_3}}\right) \quad (11)$$

An optimization algorithm was applied using this fir to optimize the parameters. For all POT inhibitors here, a monophasic dose-response curve was found.

4.7.8. Determination of K_i- and α-parameter through Lineweaver-Burk plot

In a Lineweaver-Burk plot, the reciprocal reaction velocities *v* are plotted against the reciprocal substrate concentration *[S]*, where for every inhibitor concentration a straight line is yielded[50]. As described by Breibeck *et. al* [19], the slopes *m* of the Lineweaver-Burk lines and the intercepts *t* with the ordinate can be used to calculate estimates for K_i and the α-value for further non-linear regression, where

$$\frac{1}{v_{app}} = \frac{K_M(1+\frac{[I]}{K_i})}{v_{max}} * \frac{1}{[S]} + \frac{1}{v_{max}}\left(1+\frac{[I]}{\alpha K_i}\right) = m * \frac{1}{[S]} + t \qquad (12)$$

describes the double-reciprocal plot. For further evaluation of *m* and *t*,

$$m = \frac{K_M}{v_{max}} * \frac{1}{K_i}[I] + \frac{K_M}{v_{max}} \qquad (13)$$

and

$$t = \frac{1}{v_{max}\ \alpha\ K_i}\ [I] + \frac{1}{v_{max}} \qquad (14)$$

were used. The intersection points with the ordinate in these equations yield values for $-K_i$ and $-\alpha \bullet K_i$, respectively, and allow for extraction of starting values of K_i and the α for equation (5) in section 4.7.6.

In Lineweaver-Burk plots, the slopes of the lines and the location of the intersection points enables unambiguous determination of the inhibition type. All POTs in this study exhibited an intersection point of the three lines to the left of the y-axis and below the x-axis, indicating mixed-type inhibition and a value for $\alpha < 1$. The results imply that the inhibitors bind both to the free enzyme E and to the enzyme-substrate complex ES, where the enzyme-substrate complex or subsequent species are preferred.

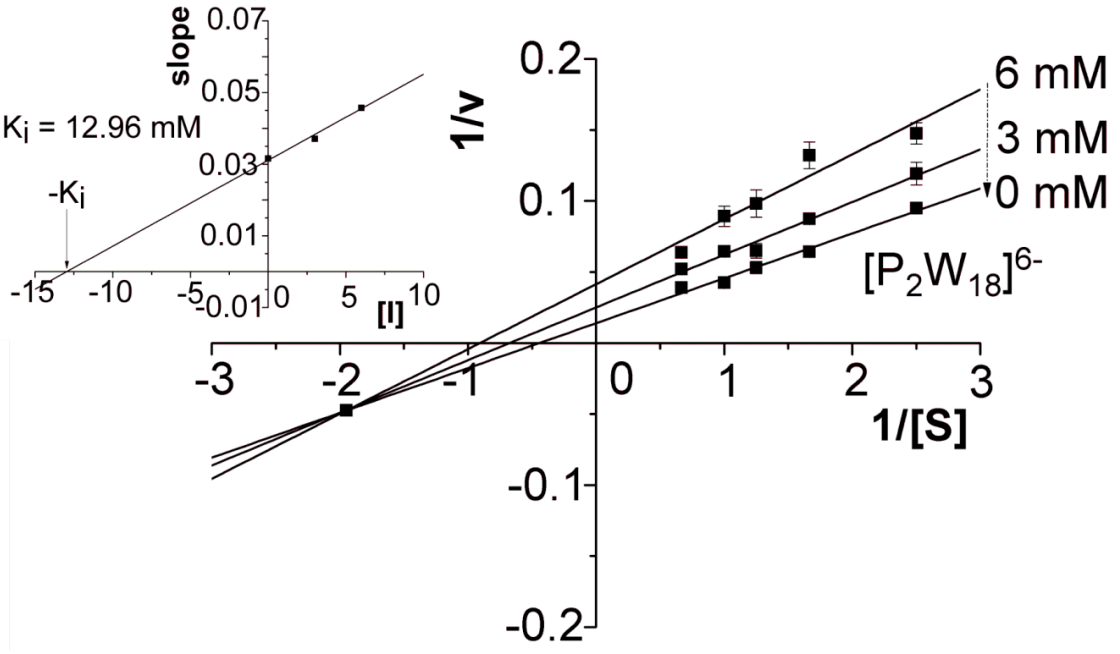

Figure S13. Kinetic evaluation of *ab*PPO4 inhibition by $[P_2W_{18}]^{6-}$ using Lineweaver-Burk plot and evaluation of K_i-value via slopes of the curves plotted against inhibitor concentration (Table S4). The plot shows the mixed-type inhibition, since the intersection point lies in the third quadrant. The inset illustrates the inhibitor concentration plotted against the slopes of the straight lines of the Lineweaver-Burk plot (Table S5).

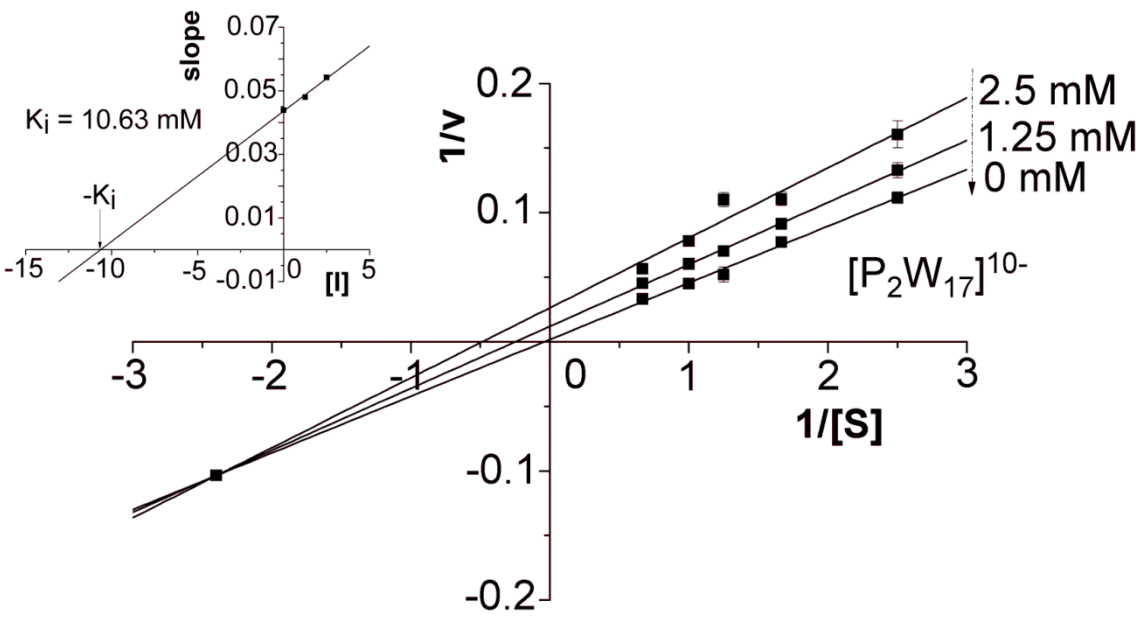

Figure S14. Kinetic evaluation of *ab*PPO4 inhibition by $[P_2W_{17}]^{10-}$ using Lineweaver-Burk plot and evaluation of K_i-value via slopes of the curves plotted against inhibitor concentration (Table S4). The plot shows the mixed-type inhibition, since the intersection point lies in the third quadrant. The inset illustrates the inhibitor concentration plotted against the slopes of the straight lines of the Lineweaver-Burk plot (Table S5).

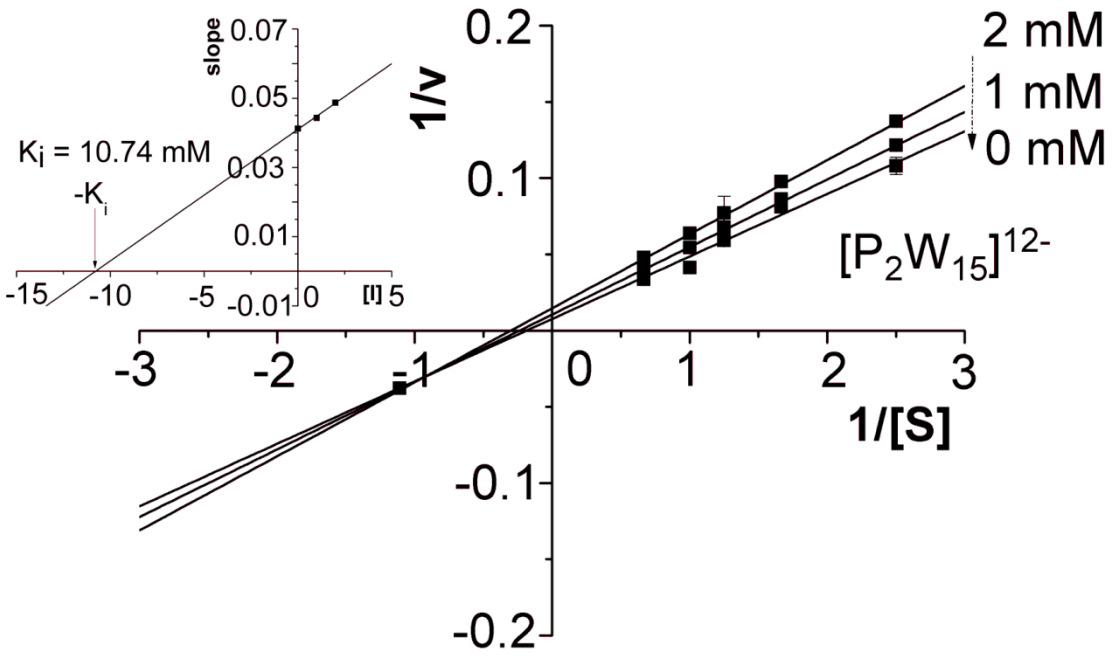

Figure S15. Kinetic evaluation of *ab*PPO4 inhibition by $[P_2W_{15}]^{12-}$ using Lineweaver-Burk plot and evaluation of K_i-value via slopes of the curves plotted against inhibitor concentration (Table S4). The plot shows the mixed-type inhibition, since the intersection point lies in the third quadrant. The inset illustrates the inhibitor concentration plotted against the slopes of the straight lines of the Lineweaver-Burk plot (Table S5).

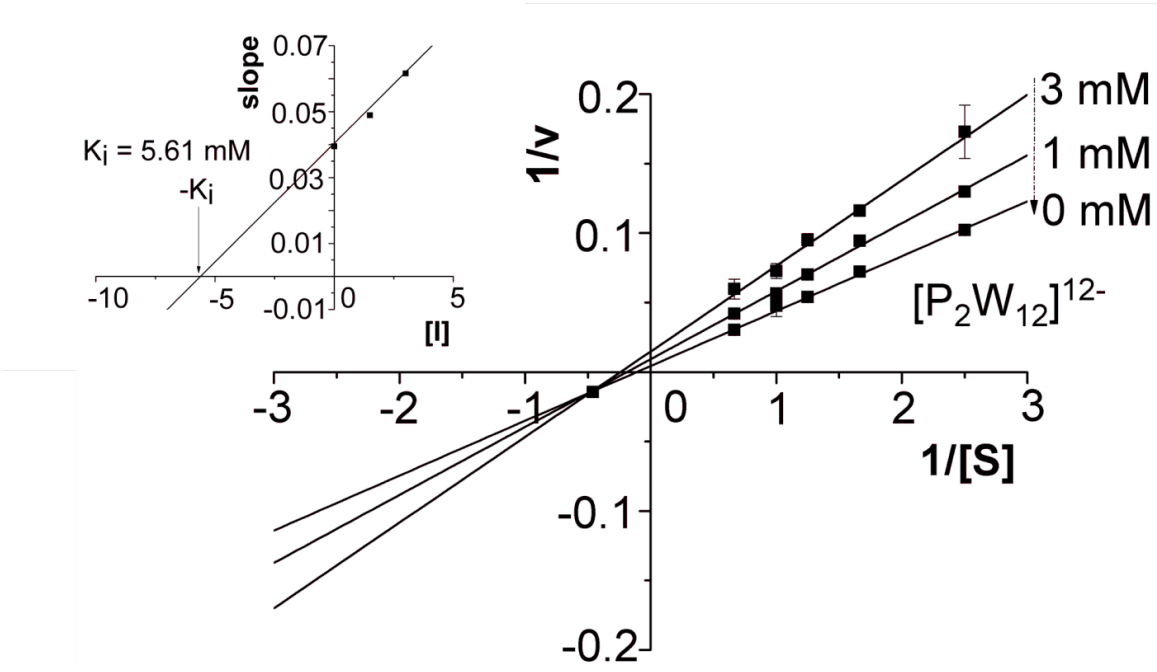

Figure S16. Kinetic evaluation of *ab*PPO4 inhibition by $[P_2W_{12}]^{12-}$using Lineweaver-Burk plot and evaluation of K_i-value via slopes of the curves plotted against inhibitor concentration (Table S4). The plot shows the mixed-type inhibition, since the intersection point lies in the third quadrant. The inset illustrates the inhibitor concentration plotted against the slopes of the straight lines of the Lineweaver-Burk plot (Table S5).

Table S4. Kinetic evaluation of Lineweaver-Burk plot. m: slope, t: ordinate intersect, R^2: line fit determination, [I]: inhibitor concentration, [S]: substrate concentration.

Inhibitor	Figure	[I]	[S]	m	t	R^2
$[P_2W_{18}]^{6-}$	S9	0 mM	0.4-1.5 mM	0.0316	0.014	0.98
		3 mM		0.0371	0.0251	0.98
		6 mM		0.0457	0.0415	0.92
	Inset	0-6 mM		0.0024	0.0311	0.98
$[P_2W_{17}]^{10-}$	S10	0 mM	0.4-1.5 mM	0.0439	0.0017	0.99
		1.25 mM		0.048	0.0119	1.0
		2.5 mM		0.0542	0.0263	0.95
	Inset	0-2.5 mM		0.0041	0.0436	0.99
$[P_2W_{15}]^{12-}$	S11	0 mM	0.4-1.5 mM	0.041	0.0077	0.99
		1 mM		0.0443	0.0106	1.0
		2 mM		0.0486	0.0147	0.99
	Inset	0-2 mM		0.0038	0.0408	0.99
$[P_2W_{12}]^{12-}$	S12	0 mM	0.4-1.5 mM	0.0395	0.0044	1.0
		1,5 mM		0.0489	0.0093	1.0
		3 mM		0.0616	0.0148	1.0
	Inset	0-3 mM		0.07202	0.0404	0.99

Table S5. Kinetic evaluation for $\alpha \cdot K_i$, m: slope, t: ordinate intersect, R^2: line fit determination, [I]: inhibitor concentration, [S]: substrate concentration.

Inhibitor	$\alpha \cdot K_i$	[I]	[S]	m	t	R^2
$[P_2W_{18}]^{6-}$	2.85	0-6 mM	0.4-1.5 mM	0.0046	0.0131	0.99
$[P_2W_{17}]^{10-}$	0.10	0-2.5 mM		0.0098	0.001	0.99
$[P_2W_{15}]^{12-}$	2.14	0-2 mM		0.0035	0.0075	0.99
$[P_2W_{12}]^{12-}$	1.58	0-3 mM		0.0034	0.005	0.98

4.7.9. Two isomers of α-$[P_2W_{17}]^{10-}$

The pH-adjusted sample $[P_2W_{12}]^{12-}$ is reported to initially rearrange towards the α_1-lacunary isomer[25] (Figure S17), and then more slowly to the thermodynamically stable α_2-isomer[51].

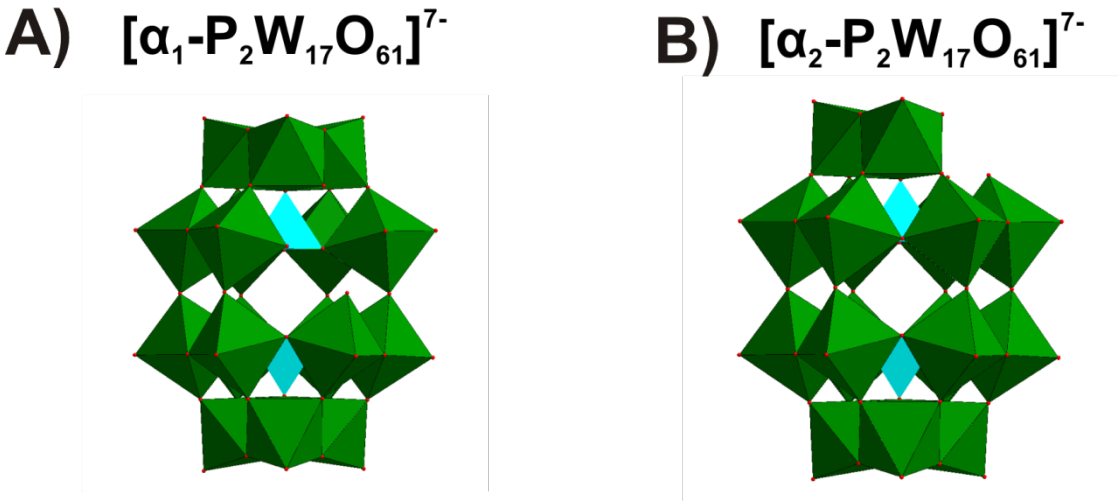

Figure S17. Two α-isomers A) & B) of $[\mathbf{P_2W_{17}}]^{10-}$ are given. $[\mathbf{\alpha_1\text{-}P_2W_{17}}]^{10-}$ has a missing equatorial {WO} group ("belt") whereas in $[\mathbf{\alpha_2\text{-}P_2W_{17}}]^{10-}$ the void is in polar position ("crown")[12]. Above pH 5 in aqueous solution, isomerization of $[\mathbf{\alpha_1\text{-}P_2W_{17}}]^{10-}$ to $[\mathbf{\alpha_2\text{-}P_2W_{17}}]^{10-}$ occurs[12]. *Colour code:* green: $\{WO_6\}$ octahedra; turquoise: $\{PO_4\}$ tetrahedron.

4.7.10. Abbreviations

Table S6. Abbreviations used in the supplementary information

Å	Ångström
ab	*Agaricus bisporus*
ACN	Acetonitril
ATP	Adenosine triphosphate
Da	Dalton
FA	Formic acid
FWHM	Full width at half maximum
HPLC	High pressure liquid chromatography
LB-media	Lysogeny broth media
L-DOPA	*L*-3,4-dihydroxyphenylalanine
LTQ	Linear Trap Quadruple
mM	Millimolar
NMR	Nuclear magnetic resonance
PMSF	Phenylmethylsulfonylfluoride
POM	Polyoxometalate
POMos	Polyoxomolybdates
POT	Polyoxotungstate
PPO	Polyphenol oxidase

5. References

[1] Mayer, A. M. & Harel, E. Polyphenol oxidase in plants. *Phytochemistry* **18**, 193-215, https://doi.org/10.106/0031-9422(79)80057-6 (1979).

[2] Mayer, A. M. Polyphenol oxidase in plants and fungi: Going places? A review. *Phytochemistry* **67,** 2318-2331, http://doi.org/10.1016/j.phytochem.2006.08.006 (2006).

[3] Fernandez, E., Sanchez-Amat, A. & Solano, F. Location and catalytic characteristics of a multipotent bacterial polyphenol oxidase. *Pigment Cell Res.* **12**, 331-339, https://doi.org/10.1111/j.1600-0749.1999.tb00767.x (1999).

[4] Rodríguez-López, J. N., Tudela, J., Varón, R., García-Carmona, F. & García-Cánovas, F. Analysis of a kinetic model for melanin biosynthesis pathway. *J. Biol. Chem.* **267**, 3801–3810, PMID:1740428 (1992).

[5] Winder, A. J. & Harris*,* H. New assays for the tyrosine hydroxylase and dopa oxidase activities of tyrosinase. *Eur J. Biochem*. **198,** 317-326, http://doi.org/10.1111/j.1432-1033.1991.tb16018.x (1991).

[6] Lima, C. R. *et al.* Combined kinetic studies and computational analysis on kojic acid analogs as tyrosinase inhibitors. *Molecules* **19**, 9591–9605, https://doi.org/10.3390/molecules19079591 (2014).

[7] Pretzler, M., Bijelic, A. & Rompel, A. fungal tyrosinases: why mushrooms turn brown. In: Reedijk, J. (Ed.) Elsevier Reference Module in Chemistry, Molecular Sciences and Chemical Engineering. Waltham, MA: Elsevier. https://doi.org/10.1016/B978-0-12-409547-2.11521-5 (2015).

[8] Mauracher, S. G., Molitor, C., Al-Oweini, R., Kortz U. & Rompel, A. Latent and active abPPO4 mushroom tyrosinases cocrystallized with hexatungstotellurate(VI) in a single crystal. *Acta Cryst.* **D70**, 2301-2315, https://doi.org/10.1107/S1399004714013777 (2014).

[9] Mauracher, S. G., Molitor, C., Al-Oweini, R., Kortz, U., & Rompel, A. Crystallization and preliminary X-ray crystallographic analysis of latent isoform PPO4 mushroom (Agaricus bisporus) tyrosinase. *Acta Cryst. **F70***, 263-266, https://doi.org/10.1107/S2053230X14000582 (2014).

[10] Mauracher, S.G. *et al.* A. High level protein-purification allows the unambiguous polypeptide determination of latent isoform PPO4 of mushroom tyrosinase. *Phytochemistry* **99**, 14-25, https://doi.org/10.1016/j.phytochem.2013.12.016 (2014).

[11] Pretzler, M., Bijelic, A. & Rompel, A. Heterologous expression and characterization of functional mushroom tyrosinase. (AbPPO4). *Sci. Rep.* **7**, srep1810, https://doi.org/10.1038/s41598-017-01813-1 (2017).

[12] Pope, M. T. Heteropoly and Isopoly Oxometalates. Springer: Berlin, Germany, 1983.

[13] Bijelic, A., Aureliano, M. & Rompel, A. The antibacterial activity of polyoxometalates: structures, antibiotic effects and future perspectives. *Chem. Commun.* **54**, 1153-1169, https://doi.org/10.1039/C7CC07549A (2018).

[14] Bijelic, A., Aureliano, M. & Rompel, A. Polyoxometalates as potential next-generation metallodrugs in the combat against cancer. *Angew. Chem. Int. Ed.* **131**, 3008-3029, https://doi.org/10.1002/ange.201803868 (2018).

[15] Bijelic, A. & Rompel, A. The use of polyoxometalates in protein crystallography – An attempt to widen a well-known bottleneck. *Coord. Chem. Rev.* **299**, 22-38, https://doi.org/10.1002/ange.201803868 (2015).

[16] Bijelic, A. & Rompel, A. Ten good reasons for the use of the Tellurium-centered Anderson-Evans polyoxotungstate in protein crystallography. *Acc. Chem. Res.* **50,** 1441–1448, https://doi.org/10.1021/acs.accounts.7b00109 (2017).

[17] Bijelic, A. & Rompel, A. Polyoxometalates - More than a phasing tool in protein crystallography. *ChemTexts* **131** 3008-3029. https://doi.org/10.1007/s40828-018-0064-1 (2018).

[18] Blazevic, A. & Rompel, A. The Anderson-Evans polyoxometalate: From inorganic building blocks via hybrid organic-inorganic structures to tomorrows "Bio-POM". *Coord. Chem. Rev.* **307** 42-64, https://doi.org/10.1016/j.ccr.2015.07.001 (2016).

[19] Breibeck, J. Gumerova, N. I. Boesen, B. Galanski, M. &. Rompel A. Keggin-type polyoxotungstates as mushroom tyrosinase inhibitors - A speciation study. *Sci Rep* **9**, https://doi.org/10.1038/s41598-019-41261-7 (2019).

[20] Briand, L. & Baronetti, G. The state of the art on Wells-Dawson heteropoly-compounds A review of their properties and applications. *Applied Catalysis A: General* **256**, 37-50 https://doi.org/10.1016/S0926-860X(03)00387-9 (2003).

[21] Gumerova; N. I. *et al.* Antibacterial activity of polyoxometalates against *Moraxella catarrhalis Front. Chem.* 6:336 https://doi.org/10.3389/fchem.2018.00036 (2018).

[22] Gumerova, N. I. *et al.* The P-type ATPase inhibiting potential of polyoxotungstates. *Metallomics* **10**, 287-295, https://doi.org/10.1039/C7MT00279C (2018).

[23] Hu, J.-J., Wang, L., Chen, B.-N., & Chi, G.-X., Transition metal substituted polyoxometalates as α-glucosidase inhibitors. *Eur. J. Inorg. Chem.* **28**, https://doi.org/10.1002/ejic.201900306 (2019).

[24] Dawson B. The Structure of the 9(18)-Heteropoly Anion in Potassium 9(18)-Tungstophosphate, $K_6[P_2W_{18}O_{62}]14H_2O$ *Acta Cryst.* **6**, 113, https://doi.org 10.1107/S0365110X53000466/ (1952).

[25] Ginsberg, A. P. *Inorganic synthesis*. **27**, 104-111, (1990).

[26] Müller, A. *et al.* „Adding“ stable functional complementary, nucleophilic and electrophilic clusters: a synthetic route to $[\{(SiW_{11}O_{39})\}]Mo_3S_4(H_2O)_3(\mu\text{-}OH)\}_2]^{10-}$ and $[\{(P_2W_{17}O_{61})Mo_3S_4(H_2O)_3(\mu\text{-}OH)\}_2]^{14-}$ as examples. *Chem. Commun.* **13**, 1189-1190, https://doi.org/10.1039/a903170g (1999).

[27] Finke, R. G., Lyon, D. K., Nomiya, K. & Weakley, T. J. R. Structure of nonasodium – triniobatopentadecawolframatodiphosphate-acetonitrile-water (1/2/23), $Na_9[P_2W_{15}Nb_3O_{62}]$

2CH_3CN 23H_2O *Acta Cryst.* **C46**, 1592-1596, https://doi.org/10.1107/S0108270190000038, (1990).

[28] Boyd, T., Mitchell, S. G., Gabb, D., Long, D.-L. & Cronin, L. Investigating cation binding in the polyoxometalate-super-crown $[P_8W_{48}O_{184}]^{40-}$. *Chem. Eur. J.* **17**, 12010-12014, https://doi.org/10.1002/chem.201101666 (2011).

[29] Mal, S. S. & Kortz, U. The wheel-shaped Cu_{20} tungstophosphate $[Cu_{20}Cl(OH)_{24}(H_2O)12(P_8W_{48}O_{184})]^{25-}$ ion. *Angew. Chem. Int. Ed.* **24**, 3777-3780, https://doi.org/10.1002/anie.200500682 (2005).

[30] Copeland, R. A. Evaluation of enzyme inhibitors in drug discovery. A guide for medicinal chemists and pharmacologists. *Methods Biochem. Anal.* **46**, 1-265, https://doi.org/10.1002/9781118540398 (2005).

[31] Lopez, X., Carbo, J.-J., Bo, C. & Poblet, J.-M. Structure, properties and reactivity of polyoxometalates: a theoretical perspective. *Chem. Soc. Rev.* **41**, 7537-7571, https://doi.org/10.1039/c2cs35168d (2012).

[32] Fuchs, J., Thiele, A. & Palm, R. *Z.* Structure and vibrational spectrum of the *α*-undecatungstophosphate $Na_2[N(CH_3)_4]_4HPW_{11}O_{39}\cdot 7H_2O$. *Naturforsch. B* **36**, 544-550, https://doi.org/10.1515/znb-1981-0504 (1981).

[33] Wang, Z.-M. *et al.* Rational modification of donepezil as multifunctional acetylcholinesterase inhibitors for the treatment of Alzheimer's disease. *Eur. J. Med. Chem.* **123,** 282-297, https://doi.org/10.1016/j.ejmech.2016.07.052 (2016).

[34] Ya-Guang, C., Gong, J., &. Lun-Yu, Q. Tungsten-183 nuclear magnetic resonance spectroscopy in the study of polyoxometalates. *Coord. Chem. Rev.* **248**, 245–260, https://doi.org/10.1016/j.cct.2003.11.003 (2004).

[35] Gumerova, N. I. & Rompel, A. Synthesis, structures and applications of electron-rich polyoxometalates. *Nat. Rev. Chem.* **2**, Art.-Nr.: 0112, https://doi.org/10.1038/s41570-018-0112 (2018).

[36] Sadakane, M., & Steckhan, E. Electrochemical Properties of Polyoxometalates as Electrocatalysts. *Chem. Rev.* **98**, 219-237, https://doi.org/10.1021/cr96043a (1997).

[37] Acerete, R., Hammer, C. F. & Baker, L. C. W. ^{183}W NMR of heteropoly- and isopolytungstates. Explanations of chemical shifts and band assignments. Theoretical considerations. *J. Am. Chem. Soc.* **104,** 5384-5390, https://doi.org/10.1021/ja00384a023 (1982).

[38] Asakura, T., Donnet, L., Picart, S. & Adnet, J.-M. Extraction of hetero polyanions, $P_2W_{17}O_{61}^{10-}$, $P_2W_{18}O_{62}^{6-}$, $SiW_{11}O_{39}^{8-}$ by TBP. *J. Radioanal. Nuclear Chem*. **246**, 651-656, https://doi.org/10.1023/A:1006795929703 (2000).

[39] Wang, J., Li, J., You, W., He, C. & Zhu, Z. Determination of the protonation state of $[H_3PW_{11}O_{39}]^{4-}$ and the stability constant of $[Ag(H_2O)(H_3PW_{11}O_{39})]^{3-}$ in aqueous solution. *J. Coord. Chem*. **69**, 2525–2531, https://doi.org/10.1080/00958972.2016.1218000 (2016).

[40] Assaf, K. *et al*. Water Structure Recovery in Chaotropic Anion Recognition: High-Affinity Binding of Dodecaborate Clusters to γ-Cyclodextrin. *Angew. Chem. Int. Ed*., **54**, 6852-6856, https://doi.org/10.1002/anie.201412485 (2015).

[41] Assaf, K. & Nau, W. The chaotropic effect as an assembly motif in chemistry. *Angew. Chem. Int. Ed*., **57**, 13968-13981, https://doi.org/10.1002/anie.201804597 (2018).

[42] Buchecker, T. *et al.* Polyoxometalates in the Hofmeister series. *Chem. Commun.*, **54**, 1833-1836, https://doi.org/10.1039/C7CC09113C (2018).

[43] Naskar, B., Diat, O., Nardello-Rataj, V. & Bauduin, P. Nanometer-Size Polyoxometalate Anions Adsorb Strongly on Neutral Soft Surfaces. *J. Phys. Chem. C*, **119**, 20985-20992, https://doi.org/10.1021/acs.jpcc.5b06273 (2015).

[44] Buchecker, T. *et al*. Self-Assembly of Short Chain Poly-*N*-isopropylacrylamid Induced by Superchaotropic Keggin Polyoxometalates: From Globules to Sheets. *J. Am. Chem. Soc.*, **141**, 6890-6899, https://pubs.acs.org/doi/10.1021/jacs.8b12181 (2019).

[45] Studier, F.W. Protein production by auto-induction in high-density shaking culteres. *Protein Expression & Purification* **41**, 207-234, https://doi.org/10.1016/j.pep.2005.01.016 (2015).

[46] Dirks-Hofmeier, M. E., Kolkenbrock, S. & Moerschbacher, B.M . Parameters that enhance the bacterial expression of active plant polyphenol oxidases. *PLoS ONE* **8**, e77291, https://doi.org/10.13171/journal.pnoe.0077291 (2013).

[47] Chen, Y.-G., Gong, J. & Qu, L.-Y. Tungsten-183 nuclear magnetic resonance spectroscopy in the study of polyoxometalates. *Coord. Chem. Rev.* **248**, 245–260, https://doi.org/10.1016/j.cct.2003.11.003 (2004).

[48] Wu, H. Contribution to the chemistry of phosphomolybdic acids, phosphotungstic acids and allied substances. *J. Biol. Chem*. **43**, 189-220 (1920).

[49] Di Veroli, G. *et al.* An automated fitting procedure and software for dose-response curves with multiphasic features. *Sci Rep* **5**, 14701, https://doi.org/10.1038/srep14701 (2015).

[50] Lineweaver, H. & Burk, D. The determination of enzyme dissociation constants. *J. Am. Chem. Soc.* **56**, 658-66, https://doi.org/10.1021/ja01318a036 (1934).

[51] Bartis, J. *et al.* Lanthanide complexes of the α_1-isomer of the $[P_2W_{17}O_{61}]^{10-}$ heteropolytungstate: Preparation, stoichiometry, and structural characterization by ^{183}W and ^{31}P NMR spectroscopy and europium(III) luminescence spectroscopy. *Inorg. Chem.* 38, 1042-1053, https://doi.org/10.1021/ic980384i (1999).

6. Appendix

6.1. Final Discussion

The POT-protein interaction principles found before could be confirmed in this study, where all the used Wells-Dawson POTs showed inhibition against *ab*PPO4. The similar shape of the kinetic curves was attributed to the stable main species $[P_2W_{17}O_{61}]^{10-}$ and its comparable charge

density with $H_3[PW_{11}O_{39}]^{7-}$, which is formed in the $[\mathbf{P_2W_{12}}]^{12-}$ sample with *L*-DOPA. The kinetic parameters were obtained by non-linear regression, with the starting values extracted from the Lineweaver-Burk plots. According to this analysis, all used POT solutions showed mixed-type inhibition.

Since the POT solutions of $[\mathbf{P_2W_{18}}]^{6-}$, $[\mathbf{P_2W_{15}}]^{12-}$ and $[\mathbf{P_2W_{12}}]^{12-}$ were structurally unstable at physiological conditions (pH 6.8) and in the presence of the substrate *L*-DOPA, the speciation of the POTs was required to indentify active POT species responsible for the observable inhibition effects. The influence of the biological pH and of the substrate has been often neglected in biological POM applications, but is crucial to understand the involved protein-inhibitor interactions.

For future inhibition studies a consideration of the choice of the substrate will be important to gain a full understanding of the inhibitory activities. To increase the hydrolytic stability of the POT inhibitors, the substitution of the intact Wells-Dawson cluster with another metal ion of lower charge is suggested to obtain *e.g.* $[P_2W_{17}O_{61}\{M(H_2O)\}]^{n-}$ with M = Co^{2+}, Ni^{2+}, Cr^{3+}, …. Moreover, such a substitution can lead to an increased protein affinity and inhibitory effect, since Breibeck *et. al.* (2019) determined a lower K_i for Ni-substituted $[PW_{11}O_{39}\{Ni(H_2O)\}]^{5-}$ (K_i = 9.7 mM) than for the intact Keggin-POT $[PW_{12}]^{3-}$ (K_i = 25.6 mM) and for the monolacunary form $[PW_{11}]^{7-}$ (K_i = 12.0 mM).

6.2. German Abstract

Alle vier getesteten POT Lösungen ($[\mathbf{P_2W_{18}}]^{6-}$, $[\mathbf{P_2W_{17}}]^{10-}$, $[\mathbf{P_2W_{15}}]^{12-}$ und $[\mathbf{P_2W_{12}}]^{12-}$) zeigten eine Inhibitionswirkung gegenüber *ab*PPO4 (K_i = 6.53 – 13.63 mM). Zur kinetischen Bestimmung der Inhibitionswirkung wurde die Catecholoxidase-Aktivität des Enzyms herangezogen. Eine Untersuchung mit Hilfe eines Hill-basierten Algorithmus ergab ein monophasisches Bindungsverhalten zwischen POT und Protein. In ^{31}P-NMR- und ^{183}W-NMR-spektroskopischen Messungen wurde $[P_2W_{17}O_{61}]^{10-}$ als die aktive Hauptspezies dieser Studie identifiziert. Diese monolacunare Form ging aus Umlagerungsprozessen der POT-Verbindungen hervor. Zusätzlich konnte für $[\mathbf{P_2W_{12}}]^{12-}$ in der Gegenwart des Substrats *L*-DOPA die vollständige Umlagerung zu $H_3[PW_{11}O_{39}]^{7-}$ beobachtet werden. Daher wurden die hydrolytische Stabilität unter biologischen Bedingungen (pH 6.8) und die Stabilität in Gegenwart von Substrat zu entscheidenden Parametern in dieser Studie. Diese Faktoren unterstreichen die Notwendigkeit der POT-Speziierung mittels NMR-Spektroskopie. Die relative Menge an $[P_2W_{17}O_{61}]^{10-}$ und die Ladungsdichte der eingesetzten Polyoxowolframate wurde für die Interpretation der erhaltenen Inhibitionskurven herangezogen. Die Abhängigkeit der Inhibitionswirkung intakter und lacunarer Wells-Dawson Polyoxowolframate auf Enzyme von der Ladungsdichte steht im Einklang mit vorausgegangenen Studien.

6.3. English Abstract

All four tested POT solutions ($[\mathbf{P_2W_{18}}]^{6-}$, $[\mathbf{P_2W_{17}}]^{10-}$, $[\mathbf{P_2W_{15}}]^{12-}$ and $[\mathbf{P_2W_{12}}]^{12-}$) showed inhibition effects against *ab*PPO4 (K_i = 6.53 - 13.63 mM). For the kinetic measurements, the diphenolase activity of the enzyme was assayed. Further investigations using a Hill-based algorithm revealed monophasic binding behavior between POT and protein. The undertaken ^{31}P-NMR and ^{183}W-NMR spectroscopic measurements identified $[P_2W_{17}O_{61}]^{10-}$ as the main active species of this study. This monolacunary form resulted from rearrangement processes of the POT compounds. Moreover, for $[\mathbf{P_2W_{12}}]^{12-}$ in the presence of substrate *L*-DOPA the full rearrangement to $H_3[PW_{11}O_{39}]^{7-}$ was observed. Therefore, the hydrolytic stability at biological conditions (pH 6.8) and stability in the presence of substrate became crucial parameters in this inhibition study. These findings support the necessity of POT speciation with NMR spectroscopy. The relative amount of $[P_2W_{17}O_{61}]^{10-}$ and the charge-density of the used POTs were used to explain the inhibitory activity of the POTs. The charge density dependence of the inhibitory effects of intact and hexavacant Wells-Dawson POTs against enzymes is in good accordance with previous studies.

6.4. List of Tables

Table 1. Summary of kinetic evaluation of *ab*PPO4 inhibition by Wells-Dawson POTs. K_i: inhibition constant. α: inhibition parameter, R^2: curve fit determination coefficient; the parameters were determined [a] from activity plot and [b] from the Lineweaver-Burk slopes or intercepts.

Table 2. Stability at physiological conditions and charge densities (*q/m*) of the Wells-Dawson POTs used. The POT species assigned to observed inhibitory capacity against *ab*PPO4 are depicted in blue.

Table S1. The mass of *ab*PPO4 was precisely confirmed by ESI-MS.

Table S2. Wells-Dawson POTs synthesized in this study and tested for inhibitory activity against *ab*PPO4. Numbered superscripts in brackets demonstrate the assignment of NMR signals to POT species in solution: (1) $[\alpha\text{-}P_2W_{18}O_{62}]^{6-}$, (2) $[\beta\text{-}P_2W_{18}O_{62}]^{6-}$, (3) $[\alpha_2\text{-}P_2W_{17}O_{61}]^{10-}$, (4) $[\alpha\text{-}PW_{11}O_{39}]^{7-}$. The Wells-Dawson POT species are reflected in certain solid state compositions of the studied samples as well. [a] solution pH for NMR spectroscopy, [b] time after solution preparation before NMR measurement, [c] POT first reported by (…), [d] POT synthesis according to (…), [e] assignment according to (…), [f] assignment according to (…).

Table S3: Summary of Keggin and Wells-Dawson POT speciation from two studies. The speciation of various Keggin POTs was taken from [19], the speciation of Wells-Dawson POTs is the result of the present study. The POT compounds (educts) undergo different structural changes upon dissolution in 50 mM Na-citrate pH 6.8 to form species (products) most stable under these conditions. Colour code: orange, not stable; yellow, partially stable; light green, stabilized by protonation; green, stable; blue, obtained under long-term reducing conditions (3 days) in the presence of 1 mM L-DOPA. The POT species assigned to observed inhibitory capacity against *ab*PPO4 are depicted in italics. It becomes obvious that POT species with a charge density close to 0.4 dominate at neutral pH and interact most strongly with the enzyme.

Table S4. Kinetic evaluation of Lineweaver-Burk plot. m: slope, t: ordinate intersect, R^2: line fit determination, [I]: inhibitor concentration, [S]: substrate concentration.

Table S5. Kinetic evaluation for $\alpha \cdot K_i$, m: slope, t: ordinate intersect, R^2: line fit determination, [I]: inhibitor concentration, [S]: substrate concentration.

Table S6. Abbreviations used in the supplementary information

6.5. List of Illustrations, Figures and Schemes

Illustration 1. Structural formula of substrate *L*-DOPA (*L*-3,4-dihydroxyphenylalanine)

Illustration 2. Overview of NMR-spectroscopy measurements without and with addition of *L*-DOPA. At pH 6.8, $H_3[P_2W_{17}O_{61}]^{7-}$ was the main species, which could be found in all samples. As predicted by the literature $[P_2W_{18}O_{62}]^{10-}$ is not stable at pH 6.8.

Figure 1. The POTs A)-D) feature the Wells-Dawson archetype and they are derived from the *α*-isomer of $[P_2W_{18}O_{62}]^{6-}$. Colour code*:* $\{WO_6\}$ octahedra, green; $\{PO_4\}$ tetrahedral, turquoise.

Figure 2. Activity plots of *ab*PPO4 with four Wells-Dawson phosphotungstates. The dopachrome assay was performed using 1 mM *L*-DOPA as the substrate in 50 mM Na-citrate buffer at pH 6.8. The measurements were taken in triplicates and a hyperbolic curve fit (equation (5), SI) was performed. The parameters are summarized in Table 1.

Figure 3. ^{31}P-NMR spectra of $[\mathbf{P_2W_{18}}]^{6-}$, $[\mathbf{P_2W_{17}}]^{10-}$, $[\mathbf{P_2W_{15}}]^{6-}$ and $[\mathbf{P_2W_{12}}]^{12-}$ at pH 6.8 (Table S3). The assignable educts and products of the hydrolytic rearrangement reactions of the respective

POTs (approximately 20 mM) under the given buffer conditions are depicted to illustrate the sample speciation. A) educt/product $H_3[P_2W_{17}O_{61}]^{4-}$ B) educts: $H_2[\alpha\text{-}P_2W_{18}O_{62}]^{10-}$ and $H_2[\beta\text{-}P_2W_{18}O_{62}]^{10-}$ on the left side; product: $H_3[P_2W_{17}O_{61}]^{4-}$ on the right side; C) product: $H_3[P_2W_{17}O_{61}]^{4-}$; D) product: $H_3[P_2W_{17}O_{61}]^{4-}$; Signal assignment according to ref.[34]. Colour code*:* $\{WO_6\}$ octahedra, white; $\{PO_4\}$ tetrahedra, blue, green, red; O atoms, red.

Figure 4. ^{31}P-NMR spectra of $[\mathbf{P_2W_{18}}]^{6-}$ and $[\mathbf{P_2W_{12}}]^{12-}$ at pH 6.8 in the presence of *L*-DOPA. The assignable educts and products of the hydrolytic rearrangement reactions of the respective POTs (approximately 20 mM) under the given buffer conditions are depicted to illustrate the sample speciation. A) product: $H_3[P_2W_{17}O_{61}]^{4-}$; B) product: $H_3[PW_{11}O_{39}]^{4-}$; signal assignment: For A) according to ref. [34], for B) according to ref. [37]. Colour code*:* $\{WO_6\}$ octahedra, white; $\{PO_4\}$ tetrahedra, pink, blue; O atoms, red.

Figure 5. The inhibitory activity of POTs is compared with the main species at pH 6.8 and at assay conditions. The intensity of the violet arrows correlates with the relative rearrangement to $H_3[P_2W_{17}O_{61}]^{7-}$ for the different inhibitors at pH 6.8. The more $H_3[P_2W_{17}O_{61}]^{7-}$ is in the sample, the higher the observed inhibitory activity of the POT. For $[\mathbf{P_2W_{12}}]^{12-}$, the Keggin archetype $H_3[PW_{11}O_{39}]^{4-}$ is the main species at assay conditions, which results in an decrease of the charge density of the POT and in an increase of the inhibitory activity. Colour code*:* $\{WO_6\}$ octahedra, green; $\{PO_4\}$ tetrahedra, turquoise.

Figure S1. A) *L*-3,4-dihydroxyphenylalanine (*L*-DOPA) was used as substrate assaying the catechol oxidase activity of *ab*PPO4. The diphenol group is oxidized to a quinone[11]. *L*-DOPA was added to $[\mathbf{P_2W_{18}}]^{6-}$, $[\mathbf{P_2W_{15}}]^{12-}$ and $[\mathbf{P_2W_{12}}]^{12-}$ for measurements with ^{31}P-NMR and ^{183}W-NMR spectroscopy (Figure 4, S9, S10). B) The competitive inhibitor kojic acid served as a reference compound with known inhibition characteristics in this study.

Figure S2. ESI-spectrum (after deconvolution) for active *ab*PPO4 after proteolytic cleavage with Proteinase K.

Figure S3. Protein sequence of *ab*PPO4 after cutting with Proteinase K; green: main domain of the enzyme to lysine (K) 382; violet: histidine (H) at the active center binding the dinuclear copper core; yellow: part of vector sequence[11].

Figure S4. SDS-PAGE of the chromatographic purification of recombinant *ab*PPO4 in its active form according to Pretzler *et al.* [11] For preparation of this figure, the gel was cropped (see Figure S5 for the original image). Lane: M: Precision Plus Protein™ Standard (BIO-RAD), 1: active *ab*PPO4: 44.5 kDa.

Figure S5. Original gel photography of the SDS-PAGE analysis shown in Figure S4. The image was taken with a Biorad Molecular Imager Gel Doc. The software used was ImageLab (version 5.2.1.) with standard settings for Coomassie-stained SDS-PAGE.

Figure S6. IR spectra of the Wells-Dawson POTs used in this study in the region of W-O-W, W-O-P and W=O bonds vibrations (1200 – 400 cm^{-1}).

Figure S7. ^{183}W-NMR of $[\mathbf{P_2W_{18}}]^{6-}$ at pH 4 (Table S2). Signal assignment according to ref. [47]. $[\alpha\text{-}P_2W_{18}O_{62}]^{6-}$ and $[\beta\text{-}P_2W_{18}O_{62}]^{6-}$ could be confirmed as stable at pH 4 as suggested by the literature (ref. [24]). *Colour code*: $[\alpha\text{-}P_2W_{18}O_{62}]^{6-}$: cap of $\{WO_6\}$ octahedra, blue; belt of $\{WO_6\}$ octahedra, red; $[\beta\text{-}P_2W_{18}O_{62}]^{6-}$: cap of $\{WO_6\}$ octahedra, petrol; belt of $\{WO_6\}$ octahedra, grey; $\{PO_4\}$ tetrahedron, white.

Figure S8. ^{183}W-NMR spectra of $[\mathbf{P_2W_{18}}]^{6-}$, $[\mathbf{P_2W_{17}}]^{10-}$, $[\mathbf{P_2W_{15}}]^{12-}$ and $[\mathbf{P_2W_{12}}]^{12-}$ at pH 6.8 (Table S2). The assignable educts and products of the hydrolytic rearrangement reactions of the respective POTs under the given buffer conditions are depicted to illustrate the sample speciation. A) educt/product: $H_3[P_2W_{17}O_{61}]^{7-}$; B) educts: $[\alpha\text{-}P_2W_{18}O_{62}]^{6-}$ and $[\beta\text{-}P_2W_{18}O_{62}]^{6-}$, product: $H_3[P_2W_{17}O_{61}]^{7-}$; C) product: $H_3[P_2W_{17}O_{61}]^{7-}$; D) product: $H_3[P_2W_{17}O_{61}]^{7-}$. Signal assignment according to ref. [47]. Rearrangement to $H_3[P_2W_{17}O_{61}]^{7-}$ was observed in all cases. *Colour code*: $[\alpha\text{-}P_2W_{18}O_{62}]^{6-}$: cap of $\{WO_6\}$ octahedra, blue; belt of $\{WO_6\}$ octahedra, red; $[\beta\text{-}P_2W_{18}O_{62}]^{6-}$: cap of $\{WO_6\}$ octahedra, petrol; belt of $\{WO_6\}$ octahedra, grey. $H_3[P_2W_{17}O_{61}]^{7-}$ $\{WO_6\}$ octahedra: top, olive green; upper belt left, dark grey; upper belt middle, lavender; upper belt right, light green; lower belt left, light blue; lower belt middle, turquoise; lower belt right, gold; bottom left, pink; bottom right, orange; $\{PO_4\}$ tetrahedra, white.

Figure S9. ^{183}W-NMR spectra of $[\mathbf{P_2W_{18}}]^{6-}$ and $[\mathbf{P_2W_{12}}]^{12-}$ in the presence of *L*-DOPA at pH 6.8 (Table S2). The assignable educts and products of the hydrolytic rearrangement reactions of the respective POTs under the given buffer conditions are depicted to illustrate the sample speciation. A) product: $H_3[P_2W_{17}O_{61}]^{7-}$; B) product: $H_3[PW_{11}O_{39}]^{4-}$; Signal assignment: for A) according to ref. [47]; for B) according to ref.[37]. Rearrangement to $H_3[P_2W_{17}O_{61}]^{7-}$ was observed in

A), and rearrangement to $H_3[PW_{11}O_{39}]^{4-}$ was observed in B). *Colour code*: $H_3[P_2W_{17}O_{61}]^{7-}$ {WO_6} octahedra: top, olive green; upper belt left, dark grey; upper belt middle, lavender; upper belt right, light green; lower belt left, light blue; lower belt middle, turquoise; lower belt right, gold; bottom left, pink; bottom right, orange; {PO_4} tetrahedron, white. $H_3[PW_{11}O_{39}]^{4-}$ {WO_6} octahedra: top and belt right, dark petrol; belt middle, light blue; belt left, dark red; bottom left, violet; bottom right, brown; {PO_4} tetrahedron, purple.

Figure S10. ^{31}P-NMR of $[\mathbf{P_2W_{18}}]^{6-}$ at pH 4 and $[\mathbf{P_2W_{15}}]^{12-}$ + *L*-DOPA at pH 6.8 (Table S2). Signal assignment for A) according to ref. [25] and for B) according to ref. [37]. A) $[\alpha\text{-}\mathbf{P_2W_{18}}]^{6-}$ and $[\mathbf{\beta\text{-}P_2W_{18}}]^{6-}$ were verified as proposed by the literature (ref. [25]). B) Most of $[\mathbf{P_2W_{15}}]^{12-}$ rearranged towards $[\mathbf{P_2W_{17}}]^{10-}$ under release of free phosphate. *Colour code:* {WO_6} octahedral, white; {PO_4} tetrahedral in $[\alpha\text{-}P_2W_{18}O_{62}]^{6-}$, green; {$PO_4$} tetrahedra in $[\beta\text{-}P_2W_{18}O_{62}]^{6-}$, red; {$PO_4$} tetrahedra in $H_3[P_2W_{17}O_{61}]^{7-}$, blue.

Figure S11. ^{183}W-NMR spectra of $[\mathbf{P_2W_{18}}]^{6-}$ after 28 d, at pH 6.8 (Table S2). Signal assignment according to ref. [25]. A) educts: $[\alpha\text{-}P_2W_{18}O_{62}]^{6-}$ and $[\beta\text{-}P_2W_{18}O_{62}]^{6-}$, product: $H_3[P_2W_{17}O_{61}]^{7-}$. B) educt/product: $[P_2W_{18}O_{62}]^{6-}$, product: $H_3[P_2W_{17}O_{61}]^{7-}$. In comparison to the measurement after 1 d, complete transformation of $[\beta\text{-}P_2W_{18}O_{62}]^{6-}$ to the α-form was discovered as the loss of corresponding signals in the spectrum. *Colour code*: $[\alpha\text{-}P_2W_{18}O_{62}]^{6-}$: cap of {$WO_6$} octahedra, blue; belt of {WO_6} octahedra, red; $[\beta\text{-}P_2W_{18}O_{62}]^{6-}$: cap of {$WO_6$} octahedra, petrol; belt of {WO_6} octahedra, grey. $H_3[P_2W_{17}O_{61}]^{7-}$ {WO_6} octahedra: top, olive green; upper belt left, dark grey; upper belt middle, lavender; upper belt right, light green; lower belt left, light blue; lower belt middle, turquoise; lower belt right, gold; bottom left, pink; bottom right, orange; {PO_4} tetrahedra, white.

Figure S12. ^{31}P-NMR - of $[\mathbf{P_2W_{18}}]^{6-}$ after 1 d and 28 d, at pH 6.8 (Table S2). Signal assignment according to ref. [25,37]. A) educts: $[\alpha\text{-}P_2W_{18}O_{62}]^{6-}$ and $[\beta\text{-}P_2W_{18}O_{62}]^{6-}$, product: $H_3[P_2W_{17}O_{61}]^{7-}$. B) educt/product: $[\alpha\text{-}P_2W_{18}O_{62}]^{6-}$, product: $H_3[P_2W_{17}O_{61}]^{7-}$. In comparison to the measurement after 1 d, an extinction of signals for $[\beta\text{-}P_2W_{18}O_{62}]^{6-}$ was discovered, demonstrating complete conversion to the α-form. *Colour code:* {WO_6} octahedra, white; {PO_4} tetrahedra in $[\alpha\text{-}P_2W_{18}O_{62}]^{6-}$, green; {$PO_4$} tetrahedra in $[\beta\text{-}P_2W_{18}O_{62}]^{6-}$, red; {$PO_4$} tetrahedra in $H_3[P_2W_{17}O_{61}]^{7-}$, blue.

Figure S13. Kinetic evaluation of *ab*PPO4 inhibition by $[P_2W_{18}]^{6-}$ using Lineweaver-Burk plot and evaluation of K_i-value via slopes of the curves plotted against inhibitor concentration (Table

S4). The plot shows the mixed-type inhibition, since the intersection point lies in the third quadrant. The inset illustrates the inhibitor concentration plotted against the slopes of the straight lines of the Lineweaver-Burk plot (Table S5).

Figure S14. Kinetic evaluation of *ab*PPO4 inhibition by $[P_2W_{17}]^{10-}$ using Lineweaver-Burk plot and evaluation of K_i-value via slopes of the curves plotted against inhibitor concentration (Table S4). The plot shows the mixed-type inhibition, since the intersection point lies in the third quadrant. The inset illustrates the inhibitor concentration plotted against the slopes of the straight lines of the Lineweaver-Burk plot (Table S5).

Figure S15. Kinetic evaluation of *ab*PPO4 inhibition by $[P_2W_{15}]^{12-}$ using Lineweaver-Burk plot and evaluation of K_i-value via slopes of the curves plotted against inhibitor concentration (Table S4). The plot shows the mixed-type inhibition, since the intersection point lies in the third quadrant. The inset illustrates the inhibitor concentration plotted against the slopes of the straight lines of the Lineweaver-Burk plot (Table S5).

Figure S16. Kinetic evaluation of *ab*PPO4 inhibition by $[P_2W_{12}]^{12-}$using Lineweaver-Burk plot and evaluation of K_i-value via slopes of the curves plotted against inhibitor concentration (Table S4). The plot shows the mixed-type inhibition, since the intersection point lies in the third quadrant. The inset illustrates the inhibitor concentration plotted against the slopes of the straight lines of the Lineweaver-Burk plot (Table S5).

Figure S17. Two α-isomers A) & B) of $[\mathbf{P_2W_{17}}]^{10-}$ are given. $[\mathbf{\alpha_1\text{-}P_2W_{17}}]^{10-}$ has a missing equatorial {WO} group ("belt") whereas in $[\mathbf{\alpha_2\text{-}P_2W_{17}}]^{10-}$ the void is in polar position ("crown")[12]. Above pH 5 in aqueous solution, isomerization of $[\mathbf{\alpha_1\text{-}P_2W_{17}}]^{10-}$ to $[\mathbf{\alpha_2\text{-}P_2W_{17}}]^{10-}$ occurs[12]. *Colour code:* green: $\{WO_6\}$ octahedra; turquoise: $\{PO_4\}$ tetrahedron.

Scheme S1: Proposed chemical equations for the structural interconversions observed in buffered solutions of Wells-Dawson POTs at pH 6.8 without *L*-DOPA ((1) – (3)) and in the presence of *L*-DOPA (equation (4)). HPO_4^{2-} was chosen as the dominating phosphate form at neutral pH, and the protonation of POT anions was neglected for simplification. However, the degree of protonation does not affect the structural scaffolds illustrated here.

7. Acknowledgments

I would like to express my gratitude to my first supervisor ***Univ.-Prof. Dr. Annette Rompel*** to offer me possibility to write my master thesis on the Institute of Biophysical Chemistry on an interesting interdisciplinary topic. I am very grateful for experiencing scientific freedom at writing my thesis.

Furthermore, I would like to thank my second supervisior ***Dr. Joscha Breibeck*** for guiding me from my practical work until writing the thesis. His sense of humor gave relief in a challenging daily routine.

I want to further thank ***Nadiia Gumerova, PhD.*** for helping me at the POT synthesis and POT speciation, who provided outstanding kindness and support.

To all members who were involved in my biochemical part like ***Dr. Aleksandar Bjelic***, ***Dr. Ioannis Kampatsikas***, ***Dipl.-Ing. Matthias Pretzler***, ***Mag. Felix Panis*** and ***Allaeddine Derardja, MSc.*** I would like to give some props, for being a helping hand if further biochemical guidance was needed.

I would like to thank ***Lukáš Krivosudský PhD., Emir Al Sayed, MSc., Elias Tanuhadi, MSc., Mag. Anatolie Dobrov*** and ***Stefan Sole, MSc.*** for providing deeper understanding in POM chemistry.

Regina Prossinagg and ***Isabella Kazada*** were always a great help if administrative and technical issues support was required.

Also, I want to thank ***my parents*** for their ongoing patience and their support in non-academic issues.